

Interplay between electron localization, magnetic order, and Jahn-Teller distortion dictates LiMnO₂ phase stability

Ronald L. Kam ^{1,2} Luca Binci ^{1,2} Aaron D. Kaplan ² Kristin A. Persson ^{1,2}
Nicola Marzari ³ and Gerbrand Ceder ^{1,2,*}

¹Department of Materials Science and Engineering, University of California Berkeley, Berkeley, California, USA

²Materials Sciences Division, Lawrence Berkeley National Laboratory, Berkeley, California, USA

³Theory and Simulation of Materials (THEOS) and National Center for Computational Design and Discovery of Novel Materials (MARVEL), École Polytechnique Fédérale de Lausanne, CH-1015, Lausanne, Switzerland



(Received 23 December 2024; revised 9 April 2025; accepted 22 May 2025; published 13 June 2025)

The development of manganese (Mn)-rich cathodes for Li-ion batteries promises to alleviate potential supply chain bottlenecks in battery manufacturing. Fundamental challenges in Mn-rich cathodes arise from phenomena such as structural changes due to cooperative Jahn-Teller (JT) distortions of Mn³⁺ in octahedral environments, Mn migration, and phase transformations to spinel-like order, all of which affect the electrochemical performance. These physically complex phenomena motivate an *ab initio* re-examination of the Li-Mn-O rock-salt space, with a focus on the thermodynamics of the prototypical, LiMnO₂ polymorphs. It is found that the generalized gradient approximation (GGA-PBEsol) and meta-GGA (r²SCAN) density functionals with empirically fitted on-site Hubbard *U* corrections yield spurious stable phases for LiMnO₂, such as predicting a phase with γ -LiFeO₂-like order (γ -LiMnO₂) to be the ground state instead of the orthorhombic (*Pmmn*) phase, which is the experimentally known ground state. Accounting for antiferromagnetic order in each structure is shown to have a substantial effect on the total energies and resulting phase stability. By using hybrid-GGA (HSE06) and GGA with self-consistent Hubbard parameters (on-site *U* and inter-site *V*) calculated from linear response theory, the experimentally observed LiMnO₂ phase stability trends are recovered. The calculated on-site *U* between Mn-3*d* states in the experimentally observed orthorhombic, layered, and spinel phases are significantly smaller than *U* in γ -LiMnO₂ and disordered layered structures, by 0.5–0.6 eV within GGA. The smaller values of *U* are shown to be correlated with a collinear ordering of JT distortions, in which all *e_g* orbitals are oriented in the same direction. This cooperative JT effect can lead to greater electron delocalization from Mn along the *e_g* states due to increased Mn-O covalency, which contributes to the greater electronic stability compared to the phases with noncollinear JT arrangements. The structures with collinear ordering of JT distortions also generate greater vibrational entropy, which helps stabilize these phases at high temperature. These phases are shown to be strongly insulating with large calculated band gaps >3 eV, which are computed using HSE06 and *G₀W₀*.

DOI: [10.1103/99jn-17v6](https://doi.org/10.1103/99jn-17v6)

I. INTRODUCTION

The manufacturing and deployment of lithium-ion (Li) batteries have experienced rapid growth, driven by their application in electric vehicles, large-scale energy storage of intermittent energy sources (e.g., wind and solar power), and personal electronic devices [1–5]. To meet the growing demand for Li-ion batteries, it is imperative that sustainable cathode chemistries based on earth-abundant elements are developed to prevent potential supply chain bottlenecks [5,6]. Manganese (Mn)-rich cathodes have emerged as strong candidates for such technologies, as Mn is significantly cheaper

and more earth-abundant than nickel (Ni) and cobalt (Co), which are the commonly used transition metals (TMs) in commercialized Li-ion batteries [6,7].

Many conventional cathode materials have been synthesized with the chemical formula LiMO₂, where *M* can be either a single species or an admixture of TMs and other metals. These are rock-salt type structures, in which the oxygen (O) sublattice is face-centered cubic (FCC) and the cations are distributed in the interstitial octahedral sites of the anion sublattice. Commonly used LiMO₂ cathode compositions are typically rich in either Ni or Co, and crystallize in a layered structure with the *R $\bar{3}m$* space group [8–10]. LiMnO₂ is particularly unique because its ground state is the orthorhombic (*Pmmn*) phase [10–12]—in contrast with the Ni and Co counterparts—and is characterized by corrugated layers of Li and Mn. This type of cation ordering is not observed as the ground state in any other reported LiMO₂ composition [10].

To date, various LiMnO₂ phases have been explored as potential cathode materials. In particular, three LiMnO₂ polymorphs have been experimentally reported: (i) the

*Contact author: gceder@berkeley.edu

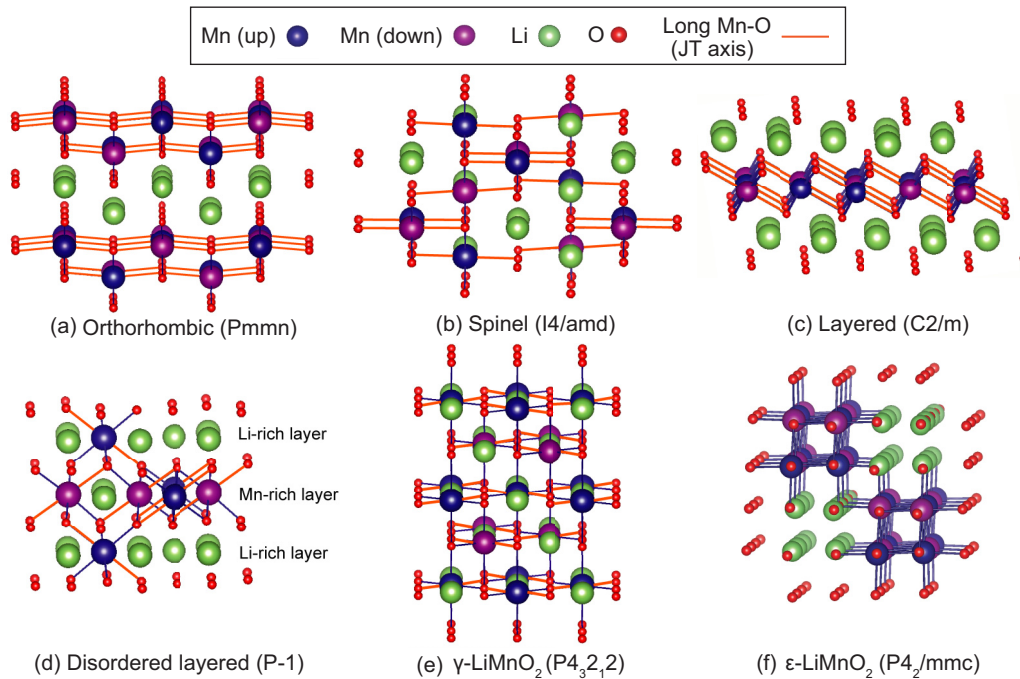


FIG. 1. Structures of the LiMnO_2 phases that are examined in this study. The majority (up, purple) and minority (down, blue) spin channels of Mn are distinguished to display the ground state AFM orderings that we identify. The long Mn-O bonds (JT axis) are shown in orange and Li-O bonds are omitted for clarity. The space groups are labeled in parentheses. The spinel phase (b) is specifically the lithiated spinel ($\text{Li}_2\text{Mn}_2\text{O}_4$ in spinel notation). In ϵ - LiMnO_2 (f), all JT axes are aligned perpendicular to the page and are not visible in the figure.

aforementioned orthorhombic ($Pmmn$), (ii) the (lithiated) spinel ($I4/amd$), and (iii) the layered ($C2/m$) phases; these are shown in Figures 1 (a)–(c), respectively [12–15]. In these LiMnO_2 phases, a Jahn-Teller (JT) distortion of Mn^{3+} occurs, characterized by the elongation of two axial Mn-O bonds and the shortening of four equatorial Mn-O bonds within the MnO_6 octahedra [16]. The direction of the (longer) axial Mn-O bonds, which we will refer to as the JT axis, are highlighted in orange in Fig. 1. The JT axes within the experimentally refined orthorhombic (ortho), spinel, and layered LiMnO_2 phases are collinearly aligned [Figs. 1(a)–1(c)] [13–15, 17–19]. The collinear ordering of JT distortions leads to a lowering of symmetry in layered LiMnO_2 ($C2/m$ space group) compared to layered LiNiO_2 and LiCoO_2 ($R\bar{3}m$ space group) [8–10]. The tetragonal symmetry of spinel LiMnO_2 (or $\text{Li}_2\text{Mn}_2\text{O}_4$ in spinel notation) also arises from the collinear ordering of JT distortions, as the delithiated states of spinel LiMn_2O_4 and λ - MnO_2 , which contain some or all Mn^{4+} , have cubic symmetry ($Fd\bar{3}m$) at ambient temperature [15, 20].

Previous experiments have indicated that these LiMnO_2 phases are thermodynamically competitive with each other. The ortho phase is experimentally known to be the ground state [12, 17], but differences in the synthesis precursors or conditions can lead to layered or spinel forming as impurity phases [21–23]. The substitution of some Mn by Al or many other metals can lead to increased stability of the layered phase [11, 24]. Phase-pure layered LiMnO_2 can be synthesized typically through ion-exchange from NaMnO_2 [13, 14]. Phase-pure spinel LiMnO_2 can be formed by lithiating spinel LiMn_2O_4 [20]. When layered or ortho- LiMnO_2 are electrochemically cycled, they tend to transform to a spinel-like phase [21–23, 25].

These experimental observations suggest that the free energy differences among these LiMnO_2 phases should be relatively small. Thus quantifying the relative stability of these polymorphs using *ab initio* calculations would provide valuable insights and is the objective of our investigation. As we will show, capturing the relative energy differences among LiMnO_2 polymorphs is complicated by the strong interplay between electron localization, JT distortions, and magnetic ordering, making this a challenging test case for modern electronic structure theory. In an early study, Mishra *et al.* showed that capturing antiferromagnetic (AFM) order and use of accurate density-functional theory (DFT) techniques are required to predict ortho as the lowest energy structure among the experimentally known LiMnO_2 phases [11]. In our study we apply a similar analysis, but using more recently developed DFT methodologies. We further investigate additional LiMnO_2 orderings that have not been experimentally reported and previously overlooked in *ab initio* studies, but that we find to have comparable energies to the known phases. These phases are the following: (i) the disordered layered phase, which is a layered structure containing 25% mixing between Li and Mn layers, (ii) γ - LiMnO_2 , which has the same cation order as the γ - LiFeO_2 phase [26], and (iii) ϵ - LiMnO_2 where Mn and Li are ordered into nearest cation neighbor Mn_4 and Li_4 tetrahedral columns. The ϵ phase is a low-energy structure that we have found from Monte Carlo simulations performed using a cluster expansion lattice model trained on the rock-salt LiMnO_2 - Li_2MnO_3 phase space (more details in Sec. VI of Ref. [27]). The disordered layered, γ , and ϵ - LiMnO_2 phases are shown in Figs. 1(d)–1(f), respectively. We note that the (DFT-relaxed) structures of disordered layered [Fig. 1(d)] and γ [Fig. 1(e)] contain JT axes that are not all collinearly

aligned, which is different from ortho, layered, spinel, and ϵ [Figs. 1(a)–1(c) and 1(f)].

In order to accurately model these LiMnO_2 phases, *ab initio* methodologies that can precisely capture the localized nature of Mn-3*d* states are needed, which presents a challenge for DFT approximations [28,29]. Specifically, the self-interaction error (SIE) [30] that is inherent to semilocal DFT approximations tends to be especially large in localized 3*d* states, and it can contribute to the overdelocalization of 3*d* electrons, incorrect prediction of metallic states in insulating TM oxides [29,31], and poor prediction of TM oxidation reaction energies [32]. To overcome these limitations, Hubbard corrections are conventionally added to generalized gradient approximation (GGA) functionals [32,33]. It has been argued early on that the key role of this Hubbard U term is to enforce piecewise linearity of the Hubbard manifold, resulting in the correction of SIE [34,35]. Within this framework, the on-site Hubbard U corrective term physically translates to a local potential constraining the electronic states projected onto the TM-3*d* manifold to be as spatially confined as possible [28,31,34,36]. In our calculations, the Hubbard U that we impose is on the Mn-3*d* manifolds, unless otherwise stated.

Besides purely on-site contributions, it has been shown that applying an additional intersite Hubbard V parameter (GGA + $U + V$)—i.e., a hybridizing interaction between TM-3*d* and O-2*p* nearest neighbors—can further improve predictions of structural, energetic, and magnetic properties in TM oxides exhibiting strong TM-O covalency [37–42]. The Hubbard parameters (HP) are generally determined either by empirical fitting of experimentally known properties (e.g., band gaps, oxidation enthalpies) [32,43,44], or from *ab initio* calculations, which can be based on linear response theory DFT [34,45–48], constrained random-phase approximation [49–51], Hartree-Fock based methodologies [41,52–54], and machine learning techniques [55–57]. When HP are obtained from empirical fitting, they are generally held constant for each TM element across all the considered structures. This scheme is frequently used, especially for high throughput workflows, as the computationally expensive calculation of HP can be avoided [32]. However, the *ab initio* calculated HP for a given species can vary significantly depending on the local environment and oxidation state [46,48,58]—variations that cannot be captured by empirical fitting procedures.

Another way of building upon the GGA functional is to incorporate electron kinetic-energy density corrections to the exchange-correlation energies, in the so-called meta-GGA functionals. Meta-GGAs, particularly the SCAN family (SCAN, rSCAN, r²SCAN), have consistently outperformed GGAs in predicting formation enthalpies and structural properties [59–65]. Kitchaev *et al.* further demonstrated SCAN’s superior accuracy in modeling the MnO_2 polymorph energetics within TM oxides [66]. Given the improved performance of SCAN and r²SCAN over GGA, Hubbard corrections are not commonly applied to these functionals, although Gautam *et al.* recently demonstrated that adding an empirically fitted Hubbard U correction to SCAN and r²SCAN can enhance the prediction of oxidation enthalpies and polymorph ground states in several TM oxides [43,44].

An alternative strategy to mitigate the self-interaction error (SIE) in generalized gradient approximations (GGAs)

involves incorporating a fraction of exact (Fock) exchange into the electronic exchange energy calculation, as implemented in hybrid functional methods [67,68]. Hybrid functionals, particularly HSE06 [69], have been demonstrated to accurately predict lattice parameters, formation energies, and band gaps of TM oxides [70–72]. For a rigorous evaluation of quasiparticle band structures, however, the *GW* method provides a more robust many-body framework, especially for the calculation of electron excitation energies [73,74]. While *GW* generally performs well for predicting band gaps of conventional semiconductors [75–77], a careful selection of the DFT starting point has to be made when dealing with TM oxides, as the accuracy of the *GW* self-energy evaluation heavily depends on the quality of the electronic ground state, especially for single-shot (G_0W_0) calculations [78,79].

In this work, we apply the DFT methods we discussed above, namely GGA + $U(+V)$, r²SCAN(+ U), and HSE06 to evaluate the phase stability of the LiMnO_2 polymorphs. The paper is organized as follows: in Sec. II, we provide the details of the computational schemes we used, while in Sec. III A, the LiMnO_2 phase stability results are presented. We find that accounting for AFM order is vital to obtain more accurate phase stability trends across several levels of theory, which is consistent with the results of Mishra *et al.* [11] and Singh [80]. We encounter challenges when applying PBEsol [81] and r²SCAN [62] with or without empirically tuned values of Hubbard U , to the various AFM LiMnO_2 phases, as the predicted ground state is the γ - LiMnO_2 phase and not the orthorhombic LiMnO_2 , which is inconsistent with experimental observations. We are thus required to assess more computationally complex schemes such as HSE06 and PBEsol with self-consistent Hubbard parameters. Using these computational methodologies, we recover relative energies in closer agreement with experiments. We assess the phase stability at elevated temperature by performing harmonic phonon calculations within PBEsol + U and determine the vibrational free energy as a function of temperature. To rationalize the differences in predicted phase stability, we analyze the properties related to the electronic structure that each method yields. Specifically, in Sec. III B, the self-consistently calculated HP in all LiMnO_2 phases and their correlation with the structural and electronic properties are examined. In Sec. III C, we analyze electronic properties such as the electron density, density of states, and band structure of ortho- LiMnO_2 across the different DFT approximations. In the absence of experimental data on the electronic structure, we present theoretical predictions of the band structure and excitation energies. Our calculations using HSE06 and G_0W_0 characterize the system as a wide band gap insulator, with the band gap estimated to be >3 eV. In Discussion (Sec. IV), we further rationalize the relation between the ion configuration, electronic structure, and phase stability trends in these polymorphs.

II. METHODS

We use a variety of DFT functionals to perform structural relaxations and calculate total energies of the LiMnO_2 phases. The Vienna *ab initio* simulation package (VASP) [82–85] is used for the structural relaxations performed within PBEsol + U , r²SCAN(+ U), and HSE06. When “+ U ” is used, a

Hubbard U is applied on the Mn-3d manifolds with values of U that have been empirically fitted in previous studies [32,44]. The pymatgen package is used to generate and manipulate structures, create calculation inputs, parse the calculation outputs [86], identify symmetries, and compute x-ray diffraction (XRD) patterns. QUANTUM ESPRESSO (QE) [87,88] is used for its implementation of extended Hubbard parameters (PBEsol + U + V) and density functional perturbation theory (DFPT) for self-consistent calculations of Hubbard U and V parameters [46,89–91]. The total energies and relaxed structures computed using these methods are openly available in the MPContribs platform [92]. The details of the DFT calculations, including the pseudopotentials, energy cutoff, and convergence criteria are listed in Sec. I of Ref. [27]. To demonstrate the consistency between the energy differences obtained with VASP and QE, we use them to evaluate the energies of the LiMnO₂ phases using PBEsol + U , scanning U from 3 to 7 eV. The results are reported in Fig. S1 [27], which show good compatibility between the two codes.

The ϵ phase was found from canonical Monte Carlo (MC) simulations at the LiMnO₂ composition, using a cluster expansion (CE) on a rock-salt Li⁺-Mn³⁺-Mn⁴⁺-O²⁻ lattice. The CE model construction and MC simulations were performed using smol [93]. More details are described in Sec. VI of Ref. [27].

The AFM ground state of each phase is identified by enumerating ~ 30 collinear AFM orderings and relaxing each structure within PBEsol + U ($U = 3.9$ eV, VASP). The AFM orderings were enumerated using the Magnetic StructureEnumerator module developed by Horton *et al.* in pymatgen [86,94]. The AFM ground state of ortho-LiMnO₂ that we identify is identical to the AFM structure that was experimentally refined by Greedan *et al.* using neutron diffraction (ND) [17].

The self-consistent calculations of the Hubbard parameters (HP) within PBEsol are performed using DFPT as implemented in the HP module of QE [90]. To converge the HP, we perform iterations in which U and V are computed using DFPT followed by a relaxation of the structure with these HP within PBEsol + U + V . This procedure is repeated until all U and V values are converged to within 10 meV between iterations. The values of the converged HP are shown and analyzed in Sec. III B. Each DFPT calculation requires the ground state electron density and wave functions, which are computed from static self-consistent field (SCF) calculations within PBEsol + U + V . We also compute the self-consistent Hubbard U within r²SCAN using QE, using the finite-difference linear response approach based on supercells [34] instead of DFPT, since the current version of QE (version 7.4) does not support DFPT calculations with meta-GGA functionals. The r²SCAN calculations in QE are performed using the interface with the Libxc library of density functionals [95]. Furthermore, we perform the self-consistent calculation of U for r²SCAN at the structural geometries relaxed using VASP, since variable-cell structural optimizations are not yet implemented for r²SCAN in QE. Due to the current limitations of the codes, we present the r²SCAN + U_{sc} results in Ref. [27]. More details of the self-consistent HP calculations are shown in Sec. II of Ref. [27].

To obtain the vibrational properties, harmonic phonon calculations are computed using the frozen phonon method with PHONOPY and VASP [84,96]. Each LiMnO₂ phase is relaxed within its respective AFM ground state and atomic displacements are generated on a supercell. The dynamical matrix is constructed by computing the forces in each supercell by performing SCF calculations. We use PBEsol + U ($U = 3.9$ eV) for the phonon calculations, as it has been previously shown that PBEsol + U can predict phonon frequencies with good accuracy in a range of TM oxides [97–100].

In Sec. III C, we compute the electronic structure of ortho-LiMnO₂ using the range of DFT functionals we have discussed, to obtain the electron density, density of states, magnetic moments, and band gaps. For these calculations, we fix the atomic positions to the primitive cell of the AFM ortho-LiMnO₂ structure that was previously refined from ND by Greedan *et al.* [17]. The band structure of ortho-LiMnO₂ is computed using PBEsol + U , HSE06, and single-shot GW (G_0W_0). SeeK-path is used to select the high symmetry path through the first Brillouin zone [101], which satisfies the magnetic symmetry of the primitive cell of AFM ortho-LiMnO₂ described by the $C2/c$ space group, which is of lower symmetry than the nonmagnetic structure ($Pm\bar{m}n$). The PBEsol + U band structure is computed using QE and its ground state wave functions are used as a starting point for the G_0W_0 calculations, which are performed using BERKELEYGW [102,103]. The single-particle Green's function (G) and screened Coulomb interaction (W) are constructed using the wave functions generated from PBEsol + U . To calculate W , the dielectric matrix (ϵ) is computed within the random phase approximation. More details are shown in Sec. V of Ref. [27].

III. RESULTS

A. LiMnO₂ phase stability

We evaluate the phase stability of the LiMnO₂ polymorphs at 0 K by performing structural relaxations and calculating the total energy using PBEsol + U , r²SCAN, and r²SCAN + U ($U(\text{PBEsol}) = 3.9$ eV [32] and $U(\text{r}^2\text{SCAN}) = 1.8$ eV [44]). Within each functional, we evaluate the energy of each structure relative to ortho-LiMnO₂ with all structures containing either FM or AFM spin ordering, as shown in Figs. 2(a) and 2(b), respectively. Hereafter, we use the notation $\Delta E_X \equiv E_X - E_{\text{ortho}}$ to represent the energy of phase X relative to ortho-LiMnO₂, where a positive value of ΔE_X implies that ortho-LiMnO₂ is lower in energy than X.

The results in Fig. 2(a) show that with FM spin order, the ortho phase is higher in energy than *all* the considered LiMnO₂ polymorphs, with the exception of ϵ . The γ -LiMnO₂ structure is clearly the ground state as $\Delta E_\gamma \approx -30$ meV/atom. Disordered layered is the second lowest in energy and is ~ 8 meV/atom below layered LiMnO₂. Layered and spinel are both predicted to be slightly lower in energy than ortho by < 5 meV/atom. The trends produced by all the applied DFT functionals are similar.

These results clearly contradict experimental observations reporting ortho as the ground state [12,17]. The prediction of γ to be the ground state is almost certainly incorrect, as the

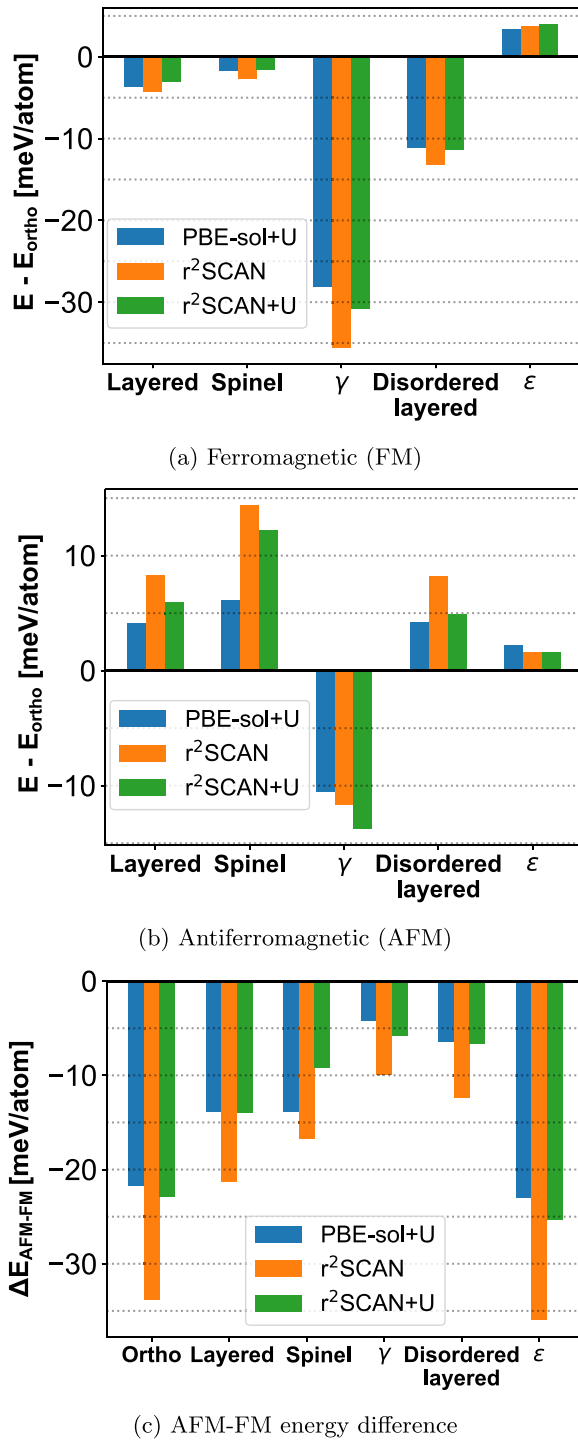


FIG. 2. DFT energy of LiMnO_2 phases relative to ortho- LiMnO_2 in the (a) FM and (b) AFM spin configurations, and (c) energy differences between the AFM and FM spin orderings ($\Delta E_{\text{AFM-FM}}$). Energies are computed with PBEsol + U ($U = 3.9$ eV), $r^2\text{SCAN}$, and $r^2\text{SCAN} + U$ ($U = 1.8$ eV) in VASP.

γ - LiFeO_2 -like cation ordering has never been reported for the LiMnO_2 composition. Furthermore, disordered layered is predicted to be lower in energy than layered, implying a negative antisite defect formation energy, which is inconsistent with the synthesis of well-ordered metastable layered LiMnO_2 [13,14].

With AFM spin ordering [Fig. 2(b)], γ remains the ground state, but its energetic advantage over the orthorhombic structure has decreased compared to the FM case [Fig. 2(a)]. The ϵ structure is again slightly higher in energy than ortho but more stable than layered and spinel. There is no significant energy difference between disordered layered and layered LiMnO_2 .

The notable differences in phase stability predicted with AFM order compared to the FM case indicate that the influence of magnetic order on the total energy varies greatly by phase, consistent with earlier findings [11]. To quantify the effect of magnetic configuration, we calculate the energy difference between the AFM and FM configurations ($\Delta E_{\text{AFM-FM}}$) for each LiMnO_2 phase and plot them in Fig. 2(c). We find that all structures are significantly more stable in their AFM ground state compared to the FM state. Ortho and ϵ are stabilized the most by AFM order, with $\Delta E_{\text{AFM-FM}} \approx -20$ to -25 meV/atom (≈ -80 to -100 meV/Mn) within PBEsol + U or $r^2\text{SCAN} + U$. While AFM order also lowers the energy of layered and spinel, ($\Delta E_{\text{AFM-FM}} \approx -10$ to -15 meV/atom) its effect is slightly smaller in magnitude than for ortho and ϵ . Within the γ and disordered layered structures, $\Delta E_{\text{AFM-FM}}$ is smaller (~ 5 meV/atom). These variations in $\Delta E_{\text{AFM-FM}}$ explain why the order of phase stability changes when all structures are in their AFM ground state compared to the FM case. We note that the absolute values of $\Delta E_{\text{AFM-FM}}$ calculated from $r^2\text{SCAN}$ are consistently larger compared to PBEsol + U and $r^2\text{SCAN} + U$. Despite this discrepancy, the qualitative trends of $\Delta E_{\text{AFM-FM}}$ among these phases are similar across these DFT approximations.

The phase stability predicted within AFM order are more consistent with experiment than in the FM case, as ortho is lower in energy than layered and spinel [Fig. 2(b)]. But certain trends are still questionable, as γ is the predicted ground state and ϵ is lower in energy than layered and spinel. Furthermore, the degeneracy of disordered layered and layered would indicate that there is no energy requirement to form specific anti-site defects in layered. We thus assess the phase stability of the LiMnO_2 polymorphs using electronic structure methods that enforce electron localization in more select ways, such as PBEsol + $U + V$ and the HSE06 hybrid functional. We also assess whether employing self-consistently calculated U and V parameters [PBEsol + $(U + V)_{\text{sc}}$] can significantly affect the results. We thus evaluate the energy of each AFM LiMnO_2 phase relative to ortho using HSE06, PBEsol + U_{sc} , and PBEsol + $(U + V)_{\text{sc}}$, with the results shown in Fig. 3.

Using these DFT functionals, we largely recover the experimental trends across all the investigated LiMnO_2 phases. HSE06 (purple bars in Fig. 3) correctly predicts the ortho phase to be the ground state of LiMnO_2 , although it is only marginally (≈ 1 meV/atom) lower in energy than γ . The ϵ structure is only slightly higher in energy than ortho ($\Delta E_{\epsilon} \approx 2$ meV/atom) and lower in energy than layered and spinel. Disordered layered becomes ~ 7 meV/atom higher in energy than layered, which corresponds to a substantial anti-site defect formation energy ($\Delta E_{\text{a-s,f}}$) of 112 meV/defect (there is one defect per $\text{Li}_4\text{Mn}_4\text{O}_8$ in disordered layered).

The phase stability predicted within PBEsol + $(U + V)_{\text{sc}}$ (green bars in Fig. 3) shares similar features with HSE06. Ortho is predicted to be the ground state. However, γ and

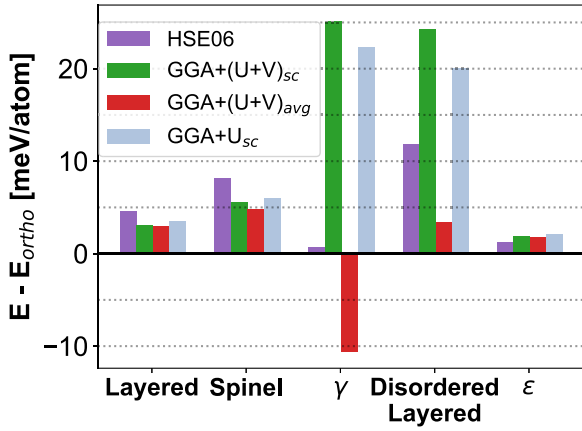


FIG. 3. DFT energy of the LiMnO_2 polymorphs relative to ortho, in their respective ground state AFM spin configurations. The functionals used are HSE06, PBEsol (GGA) with self-consistently (sc) determined U (PBEsol + U_{sc}), PBEsol + $(U + V)_{sc}$, and PBEsol with averaged (avg) $U = 6$ eV and $V = 0.6$ eV.

disordered layered are both significantly higher in energy relative to ortho ($\Delta E_\gamma \approx \Delta E_{\text{dis lay}} \approx 25$ meV/atom). This energy difference corresponds to $\Delta E_{a-s,f} \approx 400$ meV/defect in layered, which is much larger than the value predicted by HSE06. The energy of layered, spinel, and ϵ relative to ortho- LiMnO_2 are in close agreement with HSE06. If we neglect the intersite V parameter and include only the self-consistent on-site U correction (PBEsol + U_{sc} – light blue bars in Fig. 3), we find that the energy differences are very close to the PBEsol + $(U + V)_{sc}$ results. The only significant differences are that ΔE_γ and $\Delta E_{\text{dis lay}}$ are slightly smaller in PBEsol + U_{sc} compared to PBEsol + $(U + V)_{sc}$. Thus capturing the variations in self-consistent U gives the leading contribution for an accurate prediction of LiMnO_2 phase stability.

We note that we have evaluated the LiMnO_2 energetics using $r^2\text{SCAN} + U_{sc}$, as shown in Fig. S3 [27], which largely recovers the same trends as PBEsol + U_{sc} (+ V_{sc}) – namely ortho is the ground state, γ is significantly higher in energy than ortho, and disordered layered is higher in energy than layered. There are discrepancies in our linear response calculations of U within $r^2\text{SCAN}$ compared to PBEsol, primarily since DFPT and variable-cell structural relaxations within $r^2\text{SCAN}$ are not yet implemented in the current version of QE; for this reason these results are reported in Ref. [27].

The LiMnO_2 energies are also evaluated using PBEsol with averaged Hubbard parameters [PBEsol + $(U + V)_{\text{avg}}$] of $U = 6$ eV and $V = 0.6$ eV, which are roughly the average of the self-consistent U and V values across all the structures (red bars in Fig. 3). PBEsol + $(U + V)_{\text{avg}}$ yields the spurious phase stability trends that were observed in PBEsol + U and $r^2\text{SCAN}$ (+ U) [Fig. 2(b)], namely, γ is the predicted ground state and disordered layered is nearly equal in energy to layered. Therefore the self-consistently calculated and structurally informed Hubbard parameters are essential in order to obtain relative phase stability that is more consistent with experiments.

The phase stability assessed thus far has been restricted to $T = 0$ K. We include finite-temperature effects by evalu-

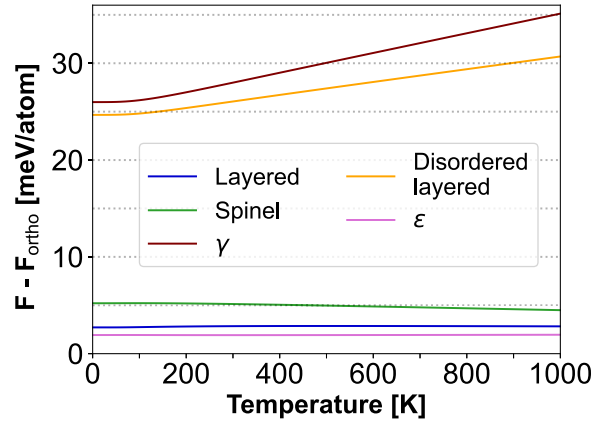


FIG. 4. Total free energy (F) relative to ortho- LiMnO_2 as a function of temperature. $F(T)$ is the sum of the vibrational free energy and DFT energy. Harmonic phonon calculations are performed within PBEsol + U ($U = 3.9$ eV) and DFT energies are computed within PBEsol + $(U + V)_{sc}$.

ating the harmonic phonon contribution to the free energy ($F_{\text{vib}}(T) = E_{\text{vib}}(T) - TS_{\text{vib}}(T)$) and adding it to the electronic PBEsol + $(U + V)_{sc}$ total energy at 0 K (E_{ele}): $F(T) = E_{\text{ele}}(T = 0) + F_{\text{vib}}(T)$. The calculated phonon density of states for each phase is shown in Fig. S5 [27]. For simplicity, we evaluate $F_{\text{vib}}(T)$ only at the PBEsol + U level in the AFM configuration. Figure 4 shows the calculated $F(T)$ of each phase relative to ortho- LiMnO_2 as a function of temperature from 0 to 1000 K (we denote $\Delta F_x(T)$ as the free energy difference of phase X relative to ortho). The free energy of ortho is lower than all the other phases across the entire temperature range considered. The experimentally observed metastable layered and spinel are only < 5 meV/atom higher in energy than ortho- LiMnO_2 across this temperature range. The ϵ phase is ≈ 2 meV/atom higher in energy than ortho and slightly lower in energy than both layered and spinel. The changes in $\Delta F_x(T)$ for layered, spinel, and ϵ are small (< 1 meV/atom) across this temperature range. For the γ and disordered layered phases, $\Delta F_x(T)$ increases significantly with temperature. Thus the vibrational entropy appears to help stabilize ortho, layered, spinel, and ϵ relative to the γ and disordered layered phases at elevated temperature.

B. Self-consistent Hubbard parameters of LiMnO_2

We have shown that the phase stability predicted with HSE06, PBEsol + U_{sc} (+ V_{sc}), and $r^2\text{SCAN} + U_{sc}$ better reflects experimental observations, compared to those obtained with PBEsol and $r^2\text{SCAN}$, with or without empirical Hubbard parameters (HPs). Specifically, all the methods with empirical or averaged HPs, whether with an on-site U or including inter-site V , yield the γ phase to be the ground state. We believe this result to be almost certainly incorrect since γ has never been experimentally reported for LiMnO_2 .

The self-consistently determined Hubbard parameters from the PBEsol + $(U + V)_{sc}$ and PBEsol + U_{sc} calculations of each phase are listed in Table I. Importantly, as shown by Timrov *et al.*, these computed HPs are not transferable across different pseudopotentials or forms of Hubbard pro-

TABLE I. Hubbard on-site U (Mn $3d$), intersite V (Mn $3d$ -O $2p$) parameters, and JT bond ratios ($\frac{\text{avg. long}}{\text{avg. short}}$) in the LiMnO₂ phases. Hubbard parameters (in units of eV) are self-consistently calculated using DFPT. Only the distinct values of each property are listed. V of the short (1.9–2.0 Å) and long (2.2–2.3 Å) Mn-O bonds are shown in separate rows. Reference values of the JT bond ratios from experimentally refined structures are listed.

Method	Property	Orthorhombic	Layered	Spinel	γ	Disordered layered	ϵ
PBEsol	U	5.81	5.79	5.81	6.36	5.92, 6.25, 6.34	5.81
+ $U + V$	V (short)	0.72, 0.59	0.65	0.66, 0.65	0.74–0.79	0.64–0.77	0.71, 0.59
	V (long)	0.38	0.30	0.31	0.57, 0.54	0.36–0.57	0.35
	JT bond ratio	1.189	1.203	1.200	1.152	1.156, 1.211, 1.138	1.190
PBEsol	U	6.01	6.01	6.02	6.49	6.08, 6.40, 6.44	6.01
+ U	JT bond ratio	1.181	1.191	1.189	1.134	1.148, 1.189, 1.125	1.181
Exp	JT bond ratio	1.182, 1.192 [17,18] 1.194 [19]	1.201 [13]	–	–	–	–

jectors, since they can have different degrees of localization [46,90]. Within PBEsol + $(U + V)_{\text{sc}}$, the self-consistent U of γ -LiMnO₂ is 6.4 eV, which is ~ 0.6 eV larger than that in ortho, layered, spinel, and ϵ -LiMnO₂ ($U \sim 5.8$ eV). In the disordered layered phase, the calculated U span a range of values (5.92–6.34 eV). Within PBEsol + U_{sc} , the trends among the calculated Hubbard U are qualitatively similar, with the key difference being that the Hubbard U parameters of each phase are systematically larger by ~ 0.17 eV on average compared to PBEsol + $(U + V)_{\text{sc}}$. Within r^2 SCAN, the values of U are ~ 4.5 eV (Table S2 [27]), which are systematically smaller by >1 eV compared to PBEsol; though we note that the differences between the Hubbard U calculated within r^2 SCAN and PBEsol arise in part due to the different pseudopotentials used (more details in Sec. II of Ref. [27]). The larger values of the calculated Hubbard U in γ and disordered layered are very likely the main reason why these phases are predicted to be unstable relative to ortho-LiMnO₂ within PBEsol + U_{sc} (+ V_{sc}) and r^2 SCAN + U_{sc} . Therefore the phase stability trends can be dictated by the nature of electron-electron interactions, which are more genuinely captured by the HPs calculated from the linear response framework.

We also observe variations in the extent of Mn JT distortions in each phase, which we measure by evaluating the ratio between the averaged long Mn-O bond length and averaged short Mn-O bond length (we will refer to this quantity as the JT bond ratio = $\frac{\text{avg. long}}{\text{avg. short}}$). Within PBEsol + $(U + V)_{\text{sc}}$, the predicted JT bond ratio of γ is significantly smaller than that of ortho, layered, spinel, and ϵ (Table I). Within disordered layered, the JT bond ratios, as well as the Hubbard U , span a range of small and large values. These trends are also observed within PBEsol + U_{sc} , which suggests that the self-consistent U and extent of JT distortion are related. The predicted JT bond ratios within PBEsol + U_{sc} are systematically smaller compared to PBEsol + $(U + V)_{\text{sc}}$, which we attribute to the increased electron localization when excluding the intersite V term. In general, the JT bond ratios predicted by PBEsol + $(U + V)_{\text{sc}}$ are in better agreement with the experimentally refined structures of orthorhombic and layered LiMnO₂ in the International Crystal Structure Database (ICSD), although the differences between PBEsol + $(U + V)_{\text{sc}}$ and PBEsol + U_{sc} are rather small.

The variations in the Hubbard parameters can also be correlated with the local electronic structure and bonding environments. We provide correlation plots between the self-consistent values of U (from PBEsol + $(U + V)_{\text{sc}}$) and Mn magnetic moments in Fig. 5(a), and the values of V with Mn-O bond length in Fig. 5(b). There is a strongly linear relation between Hubbard U and Mn magnetic moment, with a coefficient of determination $R^2 = 93.96\%$ [Fig. 5(a)]. A similar linear relation is also found for PBEsol + U_{sc} (shown in Fig. S2 [27]). This strongly linear relation between U and Mn moment indicates that the self-consistent U reflects the degree of electron localization on each Mn site. To demonstrate that the variation in Mn magnetic moments is not an artifact of the distinct values of applied HPs, we compare the Mn magnetic moments calculated using averaged HPs ($U = 6$ eV and $V = 0.6$ eV) with the Mn moments calculated using PBEsol + $(U + V)_{\text{sc}}$ in Fig. S6 [27], which shows that the magnetic moments from both methods are very close (RMSE = $0.008 \mu_B$).

The larger values of U specifically arise on Mn atoms that are part of 180° Mn-O-Mn complexes in which one Mn-O bond is long (~ 2.3 Å) and the other is short (~ 1.9 Å). In the following discussion, we will refer to a Mn taking part in this type of complex as possessing a “noncollinear” JT distortion, while the Mn that do not as having a “collinear” JT distortion. In Fig. 5(a), we see that the Mn atoms with collinear JT (green squares) have significantly smaller values of Hubbard U and magnetic moment (PBEsol + $(U + V)_{\text{sc}}$) compared to the Mn with noncollinear JT (orange crosses). In ortho, layered, spinel, and ϵ -LiMnO₂, the JT axes are all collinearly ordered (structures shown in Fig. 1), which leads to a smaller U compared to γ -LiMnO₂, in which the Mn have a noncollinear JT distortion and larger U . Given that the elongated Mn-O JT axis reflects a filled e_g orbital, the noncollinear arrangement almost certainly reflects filled-empty orbital ordering, consistent with the higher degree of localization and higher U value.

In the disordered layered phase, the mixing between Mn and Li layers leads to distinct Mn environments that include both collinear and noncollinear JT distortions in the DFT-relaxed configuration. We display the ionic and magnetic structure of disordered layered LiMnO₂ in Fig. 6, and tab-

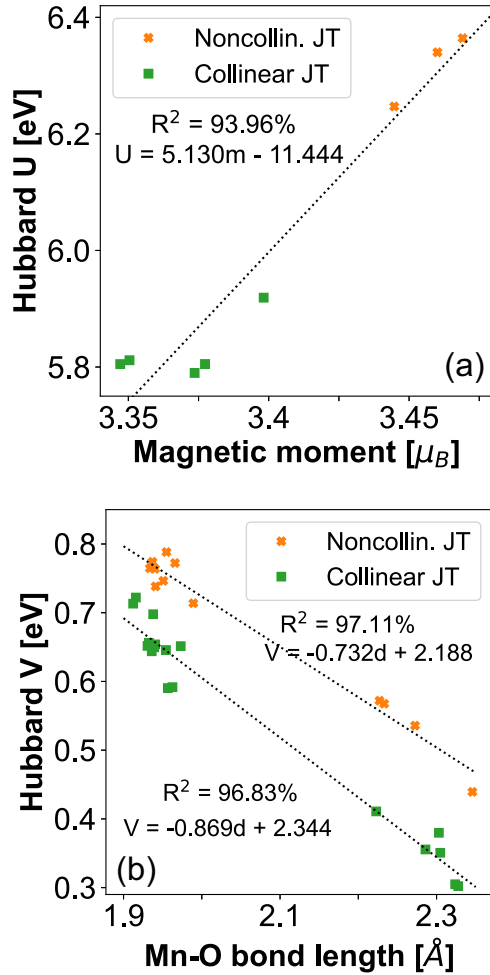
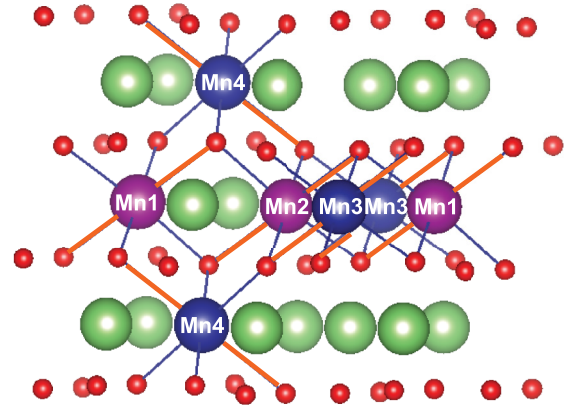


FIG. 5. Correlating self-consistent HPs from PBEsol + $(U + V)_{sc}$ with the local electronic structure and bonding environments. Plots of (a) Hubbard U with Mn magnetic moment and (b) V with Mn-O bond length. All magnetic moments and bond lengths are calculated from the self-consistent HPs. The values of HPs are distinguished by the noncollinear (orange crosses) and collinear (green squares) JT distortions. Lines of best fit and R^2 values are shown.

ulate the values of Hubbard U and magnetic moment [within PBEsol + $(U + V)_{sc}$] for each distinct Mn site. Mn1 and Mn2 only form 180° Mn-O-Li interactions, and thus we can classify these sites as having collinear JT distortions (Fig. 6). Consequently, Mn1 and Mn2 have relatively small values of U and absolute value of the magnetic moment. Mn3 and Mn4 take part in 180° Mn-O-Mn interactions with each other, in which one Mn-O bond is long and the other short—thus both have a noncollinear JT distortion. The values of U on Mn3 and Mn4 are significantly greater than that of Mn1 and Mn2.

We also observe a strongly linear correlation between V and the Mn-O bond length (d_{Mn-O}) [Fig. 5(b)]. On first glance, there appears to be a large spread in the values of V , although the trend of V with d_{Mn-O} is approximately linear with a R^2 of 80%. The values of V can be partitioned into two groups: one with Mn sites that have a noncollinear JT (orange crosses in Fig. 5(b)) and the other group consisting of Mn with collinear JT distortions [green squares in Fig. 5(b)]. Within



Mn(#)	U (eV)	Moment (μ_B)
Mn1	5.92	-3.40
Mn2	5.92	-3.40
Mn3	6.25	3.44
Mn4	6.34	3.46

FIG. 6. Structure of the disordered layered phase and table of Hubbard U and magnetic moments corresponding to each labeled Mn, calculated within PBEsol + $(U + V)_{sc}$. Mn atoms are distinguished by their spins (blue for up-spin, and purple for down-spin). Green atoms - Li, red atoms - O.

these groups, the linear fits of V as a function of d_{Mn-O} become remarkably more accurate, with $R^2 = 97\%$. The values of V associated with Mn sites that have a collinear JT are significantly smaller than the V on Mn sites with noncollinear JT, as the lines of best fit are separated by > 0.1 eV in the examined range of d_{Mn-O} . Thus the values of Hubbard U and V appear to be correlated to the local Mn-3d orbital ordering. The linear trend between V and d_{Mn-O} can be rationalized as a shorter bond length reflecting stronger binding between the Mn-3d and O-2p states, and thus leading to a larger hybridizing V value.

C. Electronic structure of orthorhombic LiMnO₂

We have observed large differences in the LiMnO₂ phase stability trends when different magnetic order and DFT approximations are applied. To rationalize these differences, we analyze the electronic structure of ortho-LiMnO₂. For these calculations, we fix the atomic coordinates to the primitive cell of the neutron diffraction refined AFM superstructure [17]. In the following discussion, the HPs imposed on PBEsol are self-consistently calculated at the experimental configuration (shown in Table III [27]), which are in good agreement with the values shown in Table I.

The electron charge density (ρ) of ortho-LiMnO₂ is computed in the AFM and FM states using PBEsol + $U + V$. The magnetic moment and band gap of these calculations are listed in Table II. We compute the difference in ρ between these two calculations ($\rho_{AFM} - \rho_{FM}$) and plot the isosurfaces in Fig. 7(a). In the AFM state, ρ increases predominantly along lobes oriented towards the Mn JT axis in the \hat{c} direction (yellow in Fig. 7), resembling e_g orbitals. The electron density also decreases (blue in Fig. 7) around Mn along the lobes that are approximately orthogonal to the JT axes, which correspond to

TABLE II. Magnetic moment of Mn and band gap of ortho-LiMnO₂ computed from self-consistent field calculations using various DFT functionals (QUANTUM ESPRESSO). AFM order is used, unless otherwise stated.

Property	PBESol	PBESol + <i>U</i>	PBESol + <i>U</i> + <i>V</i>	PBESol + <i>U</i> + <i>V</i> (FM)	PBESol + <i>U</i> _{Mn,O} + <i>V</i>	HSE06
Mn moment (μ_B)	3.00	3.38	3.32	3.35	3.43	3.26
Band gap (eV)	0.9	1.6	2.0	1.2	2.5	3.1

t_{2g} -like states. Thus there appears to be a rearrangement of ρ near Mn, such that electrons are removed from t_{2g} orbitals and fill the e_g orbitals. The shape of the positive isosurface along the e_g states is more diffuse compared to the more localized t_{2g} orbitals, indicating a more pronounced covalency between Mn and the neighboring O along the JT axis. This increased covalency is reflected in the slightly lower Mn magnetic moment in the AFM state (3.32 μ_B) compared to the FM case (3.35 μ_B) (Table II). We also observe significant rearrangement of ρ near each O site, as ρ is decreased from lobes that are oriented along \hat{c} having a $2p$ -orbital shape, and ρ is increased along the $2p$ -like lobes oriented along [110]. The AFM order also leads to a significantly larger band gap compared to FM (2.0 and 1.2 eV, listed in Table II). These substantial changes in electronic structure driven by altering the magnetic order should contribute to the large energy differences calculated using different spin configurations.

To understand the differences between the DFT methods considered, we perform SCF calculations of AFM ortho-LiMnO₂ using PBESol, PBESol + *U*, PBESol + *U* + *V*, PBESol + *U*_{Mn,O} + *V*, and HSE06, where *U*_{Mn,O} refers to a Hubbard *U* imposed on both the Mn-3*d* and O-2*p* manifolds. The Mn magnetic moment and band gap calculated using each method are presented in Table II. The band gaps increase from PBESol to PBESol + *U*, to PBESol + *U* + *V*,

to PBESol + *U*_{Mn,O} + *V*. The magnetic moments do not increase in the same order, as *V* tends to penalize larger on-site moments. However, all the magnetic moments lie within a reasonable range of each other, from 3 μ_B with PBESol to 3.43 μ_B with PBESol + *U*_{Mn,O} + *V*.

The energy levels and orbital character of the electronic states can provide insights about the degree of electronic hybridization and localization. The projected density of states (pDOS) from the scf calculations on ortho-LiMnO₂ are shown in Fig. 8. We examine the energy range from 0 to -8 eV relative to the Fermi level (E_F - which we refer to as the highest occupied energy level) and contains the band manifolds that are mostly Mn-3*d* and O-2*p* in character.

In the calculation using PBESol, the states in the region between 0 to -2 eV are predominantly Mn-3*d* in character Fig. 8(a). The pDOS spectrum shows a sharp peak in the region between -1 to -2 eV, which indicates that these Mn-3*d*-like bands are relatively flat and unhybridized (the PBESol band structure is shown in Fig. S4 [27]). When an on-site *U* is added (PBESol + *U*), these top valence states become significantly more O-2*p* in character, while the states at lower energy (-5 to -7 eV) become more Mn-3*d* in character [Fig. 8(b)]. Thus the on-site *U* shifts the O-2*p* states higher in energy relative to Mn-3*d*. The peaks in the pDOS at -1 to -2 eV that are observed in PBESol [Fig. 8(a)] are not present in PBESol + *U* [Fig. 8(b)], which indicates that these bands have greater dispersion when *U* is applied. Indeed, it can be seen from plots of the band structure that between -1 to -2 eV, the PBESol bands (Fig. S4 [27]) are flatter than PBESol + *U* (Fig. 9). The pDOS spectrum computed within PBESol + *U* + *V* [Fig. 8(c)] is similar to PBESol + *U*, with the main difference being the increase in band gap when adding the inter-site *V* term (2.0 eV compared to 1.6 eV in PBESol + *U*).

When HSE06 is employed, the manifold of states in the region between 0 to -1 eV becomes separated from the rest of the states that are lower in energy [Fig. 8(d)]. We assign the states in the 0 to -1 eV region to represent the e_g orbitals, while the states lower in energy to be the t_{2g} orbitals, which would be consistent with the crystal field theory of transition metal octahedral complexes. Within this picture, the energy separation between e_g and t_{2g} states represents the crystal field splitting energy (ΔE_{cf}). Within HSE06, the t_{2g} states (from -5 to -7 eV) have slightly more O-2*p* character than Mn-3*d*, and the difference between the two is nearly uniform along the entire energy range. The more uniform distribution of Mn-3*d* and O-2*p*-like states in HSE06 suggests an increased Mn-O hybridization and covalency.

The r^2 SCAN + *U* pDOS [Fig. 8(e)] shows a band gap (1.7 eV) that is substantially smaller than the HSE06 band gap (3.1 eV). However, the occupied manifold of r^2 SCAN + *U* is

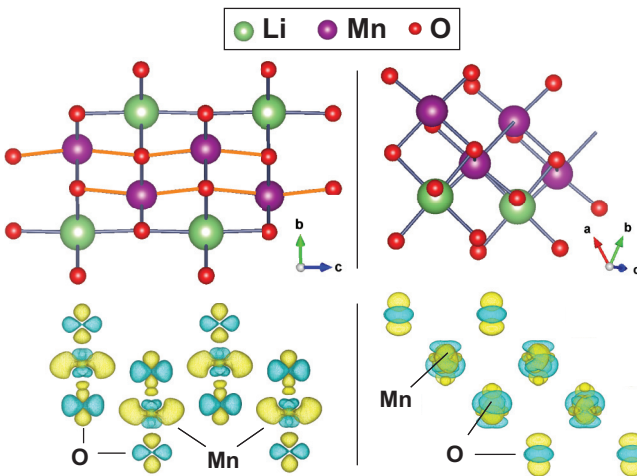


FIG. 7. Isosurfaces of the difference in charge density (ρ) between FM and AFM states of ortho-LiMnO₂ [$\rho(\text{AFM}) - \rho(\text{FM})$] computed within PBESol + *U* + *V*, visualized at two different crystal orientations as shown in the top panels. The yellow (blue) regions indicate areas of increased (decreased) ρ in the AFM structure. The bonds highlighted in orange correspond to the long bond (~ 2.3 Å) in the Jahn-Teller complex.

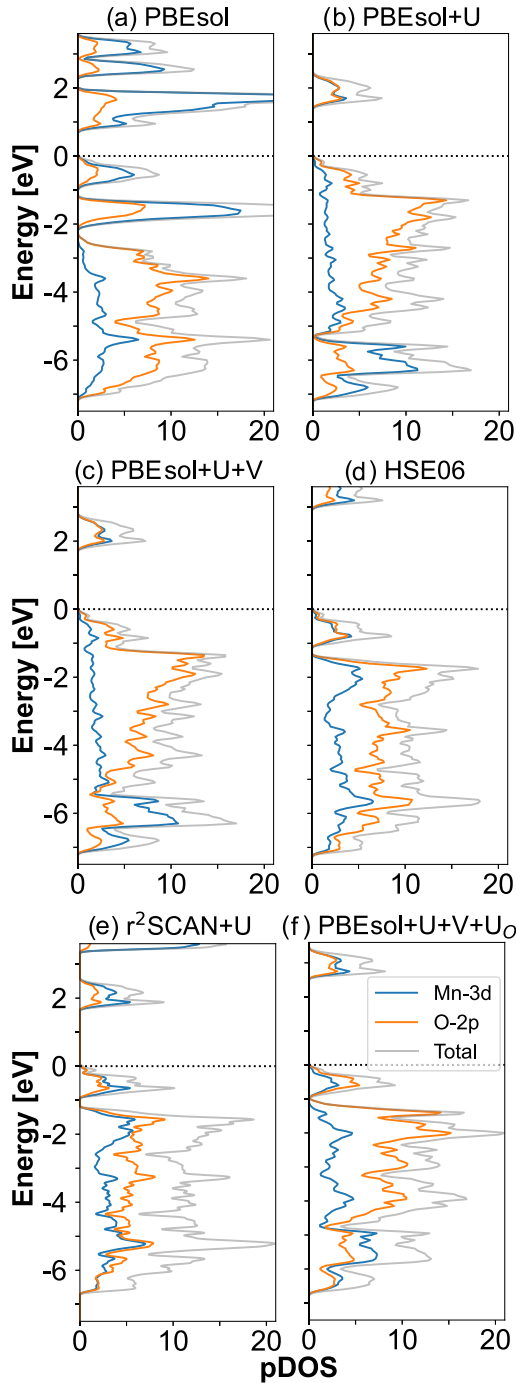


FIG. 8. Projected density of states (pDOS) of ortho-LiMnO₂ computed using (a) PBEsol, (b) PBEsol + U , (c) PBEsol + U + V , (d) HSE06, (e) r²SCAN + U , and (f) PBEsol + $U_{\text{Mn,O}}$ + V . Blue: Mn-3d, orange: O-2p, and grey: total DOS. Energies are referenced to E_{F} .

in striking agreement with HSE06; in particular, both r²SCAN + U and HSE06 display energetically separated e_g and t_{2g} states (i.e. a nonzero ΔE_{cf}) – a feature that is not present neither in PBEsol + U nor in PBEsol + U + V . Interestingly, within PBEsol, a nonvanishing ΔE_{cf} can be recovered by applying an additional Hubbard U on the O-2p states [see Fig. 8(f), PBEsol + $U_{\text{Mn,O}}$ + V]. Thus the manifestation of the

crystal field splitting appears to be intimately related to the electronic localization on O-2p states.

Since we have assessed a large array of DFT methods, it is important to evaluate the accuracy of each approximation. Given a lack of experimental data on the electronic structure of ortho-LiMnO₂, we perform a G_0W_0 calculation as a reference point for a realistic description of the electronic structure. The band structure of ortho-LiMnO₂ is computed using PBEsol + U , G_0W_0 , and HSE06, which are all shown in Fig. 9. The bands of the majority and minority spin channels are degenerate. To display the differences between the electronic states calculated within G_0W_0 and its PBEsol + U starting point (i.e., the self-energy corrections), we reference the band energies of these two calculations to E_{F} of the PBEsol + U calculation in Figs. 9(a) and 9(b).

Within G_0W_0 [Fig. 9(b)], we observe a large renormalization of the PBEsol + U band energies [Fig. 9(a)], with self-energy corrections on the order of 1 eV in magnitude, though the values of the self-energies are highly dependent on the band and wave vector. The two empty e_g conduction bands are rigidly shifted upward in energy by ~ 1.2 eV and the valence bands are shifted down by up to > 1 eV compared to PBEsol + U [Fig. 9(a)], leading to a significantly larger band gap (3.8 eV) compared to PBEsol + U (1.6 eV). There are more band crossings in the t_{2g} manifold within G_0W_0 , which highlights the larger dispersion of these bands compared to PBEsol + U . The crystal field splitting ΔE_{cf} is ~ 0.3 eV between the e_g and t_{2g} bands. In PBEsol + U , ΔE_{cf} vanishes as an e_g and t_{2g} band are degenerate at Γ [Fig. 9(a)], which is consistent with the PBEsol + U pDOS of Fig. 8(a). The values of ΔE_{cf} and the e_g band widths in G_0W_0 are close to those in the HSE06 band structure [Fig. 9(c)] and r²SCAN + U DOS [Fig. 8(f)], which validates the electronic structure of the valence states predicted by these DFT functionals.

IV. DISCUSSION

In this study, we have computed the total energy of the LiMnO₂ polymorphs using several DFT methods and evaluated harmonic phonon contributions to the free energy at finite temperature. Obtaining accurate phase stability trends is not trivial in this system, as precise description of the AFM order and interplay between electronic localization/hybridization are required. These effects are inadequately treated within more conventional DFT functionals (e.g., PBEsol + U , r²SCAN, and r²SCAN + U , where values of U are empirically tuned), which lead to the spurious prediction that γ -LiMnO₂ is the ground state. Instead, DFT schemes such as HSE06, PBEsol + U_{sc} (+ V_{sc}), and r²SCAN + U_{sc} are needed to recover ortho-LiMnO₂ as the ground state. Furthermore, these functionals are necessary to predict a disordered layered ordering to be higher in energy than the layered phase, which represents an appreciable anti-site defect formation energy in layered.

We find that an important aspect of the energy difference between all structures arises from the local variation of self-consistently determined Hubbard parameters, especially the on-site U , which is why schemes with averaged Hubbard parameters cannot reproduce the correct phase stability. Specifically, the self-consistent U and V are smallest

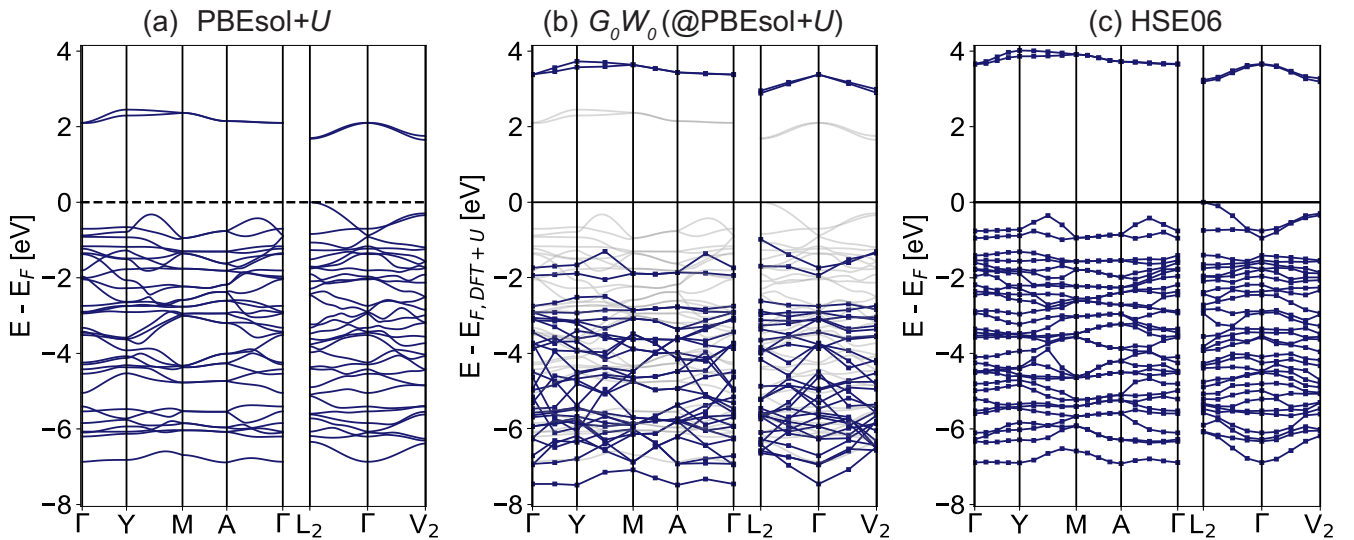


FIG. 9. Electronic band structure of the ND-refined AFM ortho-LiMnO₂ structure, computed using (a) PBEsol + U , (b) G_0W_0 starting from the PBEsol + U wave functions, and (c) HSE06. The majority and minority spin channels are degenerate. In (b), the band energies are referenced to the E_F calculated from PBEsol + U and the PBEsol + U band structure is shown in light grey to highlight the G_0W_0 self-energy corrections. Marked squares in (b) and (c) indicate the points where the band energies are computed and the lines are linear interpolations between them.

in the ortho, layered, spinel, and ϵ phases (Table I). These phases all exhibit a collinear ordering of the JT distortions, in which all of the JT axes (and hence the e_g orbitals) are oriented in parallel. Capturing these local variations in electronic interactions in DFT is key for obtaining accurate energetics in this system, and likely would be important for modeling other TM oxides rich in Mn³⁺ or other JT-active ions (e.g., Ni³⁺ and Cu²⁺). HSE06 can also reasonably capture these local differences in the electron-electron interactions despite not explicitly applying these Hubbard corrections, as it predicts orthorhombic to be the LiMnO₂ ground state. Range-separated hybrid functionals such as HSE06 more rigorously treat the screened electronic exchange interactions as they incorporate a fraction (0.25 in HSE06) of exact Fock exchange to the short-range exchange energy, which can provide an adequate correction to the self-interaction error (SIE) [69,70]. This indicates that a major source of the errors encountered in applying PBEsol + U and r^2 SCAN (+ U) is the poor description of electronic exchange, which can be remedied by calculating the HP self-consistently.

The differences in formalism of the hybrid-GGA and GGA with self-consistent HPs lead to a different phase stability trend between the γ and ortho phases: within HSE06, γ is only marginally higher in energy (~ 1 meV/atom, Fig. 3) than ortho-LiMnO₂, while PBEsol + U_{sc} (+ V_{sc}) predict a much larger energy difference (>20 meV/atom). It is difficult to conclude which method is most accurate for this quantity, as there is no known experimental measurement. However, we note that within HSE06, we apply values of the fraction of exact exchange ($\alpha = 0.25$) and range-separation parameter ($\omega = 0.2$) that may not be the optimal values for each LiMnO₂ phase. Methods have been proposed to nonempirically and systematically tune the parameters within hybrid-GGA func-

tionals to more realistically describe the electronic screening and/or minimize the SIE within a given structure [104–107] – in the same spirit as the calculation of HPs from linear response [34,37]. Thus it may be insightful in future studies to evaluate the LiMnO₂ phase stability using a nonempirically tuned hybrid-GGA, though this would come at larger computational cost.

The improved treatment of electronic exchange within HSE06 enables it to more accurately predict the band structure of ortho-LiMnO₂, as it shows reasonable agreement with the many-body G_0W_0 method, especially in the band gap and crystal field splitting (ΔE_{cf}) (Fig. 9). These quantities are more poorly described within PBEsol + U_{sc} (+ V_{sc}), which we have attributed to an insufficient correction of SIE on O-2 p states, which can be alleviated by applying an additional Hubbard U correction on O-2 p states (U_O), r^2 SCAN + U , or HSE06. The values of U_O that we calculate from DFPT are ~ 9 eV (Table S3 [27]), which are larger than the U values of Mn (~ 6 eV), but in good agreement with previous self-consistent calculations of U_O within GGA functionals [48,108]. The G_0W_0 and HSE06 methods predict large band gaps (3.8 and 3.1 eV, respectively) that are significantly higher than previously reported calculations [11,80,109–111], and indicate that these phases are strongly insulating.

The electronic structure of these phases are heavily linked to the magnetic order, as the AFM order is shown to increase the covalency of Mn-O bonds, which likely contributes to the significant lowering of energy in each AFM structure relative to the FM state [Fig. 2(c)]. This enhancement in the hybridization between the Mn-3 d and O-2 p states is correlated with an improved prediction of phase stability [Fig. 2(b)]. Correlation between AFM interactions and Mn-O covalency is consistent with the theory of AFM “semicovalent exchange,” which was

initially developed by Goodenough and Loeb to rationalize the antiferromagnetism of various spinel and perovskite phases [112–114]. Within this theory, a local AFM interaction would lead to the formation of semicovalent bonds between a TM and anion [112,113,115,116]. The large energy difference between FM and AFM states in the ortho and ϵ structures [$\Delta E_{\text{AFM-FM}} \approx -80$ to -100 meV/Mn, shown in Fig. 2(c)] suggests that the semicovalent exchange is particularly strong in these phases and is an important factor that helps stabilize them relative to the other LiMnO₂ phases. The ion configurations of ortho and ϵ -LiMnO₂ (Fig. 1) contain 90° and 180° Mn-O-Mn channels for AFM interactions, whereas layered and spinel only have 90° Mn-O-Mn channels. This structural difference may be why AFM order can have a stronger stabilizing effect on ortho and ϵ compared to the other experimentally observed layered and spinel phases.

Despite the disparity of phase stability trends observed across different DFT functionals, the energy differences between the experimentally known ortho, layered, and spinel LiMnO₂ phases are surprisingly consistent across each method, which suggests a similarity in the electronic structure of these phases. The PBEsol + $U(+V)$, r²SCAN (+ U), and HSE06 functionals all predict that the order of DFT total energy from low to high energy is ortho → layered → spinel, when all structures are in their respective AFM ground state [Figs. 2(b) and 3]. The energy relative to ortho is 5–15 meV/atom for spinel and 3–8 meV/atom for layered, depending on the functional used. The vibrational free energy of these phases between $T = 0$ to 1000 K are also very similar (Fig. 4). These observations theoretically confirm that these phases are very thermodynamically competitive across a wide range of temperatures. This thermodynamic competition elucidates why many experimental procedures to synthesize ortho LiMnO₂ can lead to spinel and/or layered impurity phases [21–24]. Since the energy differences at the LiMnO₂ composition are small, minor off-stoichiometry in Li or Mn content could possibly lead to changes in the phase stability. If this is the case, then the presence of impurity phases may be a result of particles containing off-stoichiometry or following a somewhat different synthesis path. Indeed, it has been previously shown from experiment and computation that upon delithiating layered or ortho LiMnO₂, there is a driving force to form the spinel phase (see Fig. S9) [11,25,117–120].

Our calculations reveal that the previously unreported ϵ -LiMnO₂ is a potential low-energy phase, since it is predicted to have an energy comparable to all of the experimentally known phases across all levels of DFT assessed. Specifically, the ϵ structure is consistently predicted to be only ~ 2 meV/atom higher in energy than ortho and lower in energy than layered and spinel. These results may be surprising, as the ϵ cation ordering has never been reported. The low energy of the ϵ phase can be rationalized from its similarities in its structural and electronic properties with ortho, layered, and spinel. Namely, we have shown that ϵ has a collinear ordering of JT axes, comparable Mn magnetic moment, and similar self-consistent Hubbard parameters to these phases.

To further evaluate the structural similarity of the ortho and ϵ phases, we compute their XRD patterns, which are shown in

Figs. 10(a) and 10(c), respectively. Both ϵ and ortho-LiMnO₂ share the same high intensity peaks at $2\theta = 15^\circ, 25^\circ, 39^\circ, 45^\circ,$ and 62° . The key differences in these patterns are in the disappearance of one of two peaks at 37° for ϵ , and different relative intensities among the peaks between 35 – 45° . While a low energy above the ground state is no guarantee for synthesizability [121], its similar diffraction pattern compared to ortho may have led ϵ to be missed in previously reported LiMnO₂ samples.

The γ phase is predicted to be the ground state within the PBEsol and r²SCAN functionals, with or without averaged Hubbard corrections [Figs. 2(a) and 2(b)]. Since the γ ordering has never been reported in the LiMnO₂ composition from experiment, we would expect it to be higher in energy than the experimentally found phases. We simulate the XRD pattern of γ and display it in Fig. 10(e), which clearly does not resemble the XRD patterns of ortho, layered, or spinel [Figs. 10(a), 10(b), and 10(d), respectively]. Thus γ would almost certainly not be mistaken for either of these phases, unlike the case of ϵ . The γ structure corresponds to the cation ordering with the lowest electrostatic energy among LiMO₂ rock salt structures [10]. Hence, the spurious LiMnO₂ ground state prediction is an indication that these methods inadequately capture the specific energy contributions that stabilize ortho-LiMnO₂, and instead overly stabilize electrostatically favorable configurations. Our results show that the phase stability and electronic structure of LiMnO₂ are more strongly influenced by the subtle balance between electron localization and hybridization, instead of electrostatics. The HSE06, PBEsol + $U_{\text{sc}}(+V_{\text{sc}})$, and r²SCAN + U_{sc} methods appear to provide a more faithful treatment of these aspects, enabling them to correctly predict ortho-LiMnO₂ as the ground state.

Our phonon calculations reveal that γ becomes more unstable relative to ortho as temperature is increased (Fig. 4), due to its lower vibrational entropy. Disordered layered is also destabilized by its lower phonon entropy, but to a smaller extent than γ . Since γ and disordered layered are the only phases considered that contain noncollinear arrangements of JT distortions, we speculate that the vibrational properties are closely linked to the degree and type of cation and orbital ordering. To further investigate this correlation, we generate a disordered LiMnO₂ special quasi-random structure (SQS) (methods described in Sec. VI of Ref. [27]) [122,123] and compare the structural and vibrational properties to the aforementioned LiMnO₂ phases. Upon structural relaxation within PBEsol + U , SQS-LiMnO₂ contains a noncollinear arrangement of JT distortions (structure shown in Fig. S7 [27]). We compute the phonon entropy (S_{ph}) of SQS-LiMnO₂ as a function of temperature and compare it to the other phases, as presented in Table III (also plotted in Fig. S8 [27]). At 300 K, SQS-LiMnO₂ has a very comparable S_{ph} compared to disordered layered and γ . These three phases have a noticeably lower S_{ph} (by 0.3–0.5 k_B /f.u.) compared to ortho, layered, spinel, and ϵ -LiMnO₂, which have very similar S_{ph} at 300 K (within 0.05 k_B /f.u. of each other). These trends are consistent across the temperature range examined. These findings suggest that only certain cation configurations can favor the formation of collinear e_g orbital arrangements, which in turn contributes to increasing the S_{ph} .

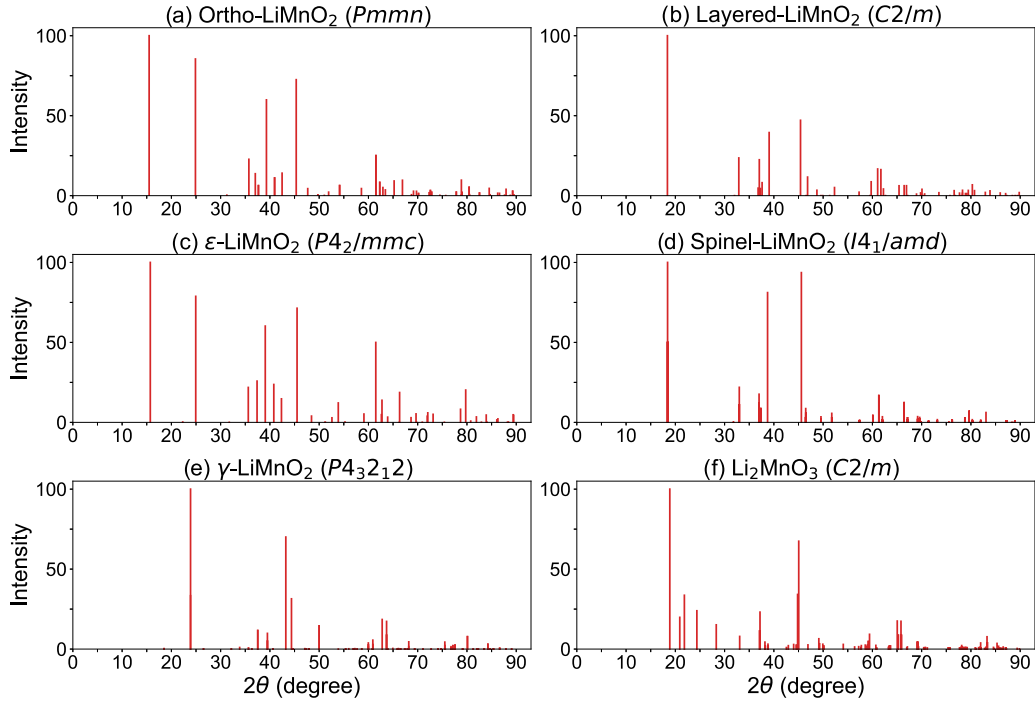


FIG. 10. Simulated XRD ($\text{Cu K}\alpha$ radiation) patterns of LiMnO_2 and Li_2MnO_3 phases. Each structure is relaxed within HSE06 and the identified space group of the final structure is shown in parentheses.

Since orthorhombic LiMnO_2 is the ground state and also exhibits relatively large S_{ph} , the collinear JT ordering appears to provide a unique source of both electronic and vibrational stability. We speculate that the relatively softer phonon modes in these structures can arise from increased phonon anharmonicity [124] and/or electron-phonon (el-ph) coupling [97,125], effects that are associated with cooperative JT distortions [16,126–128]. Although our employed frozen phonon method does not explicitly account for anharmonicity and el-ph coupling, it may capture small contributions from these effects.

Our findings also indicate that the degree of electron localization and hybridization can be affected by the ordering of JT distortions, as shown by our identification of large variations in self-consistent HPs. The self-consistent Hubbard U in γ is significantly larger than that of the experimentally known phases (Table I). The values of U are shown to linearly correlate with the Mn magnetic moment [Fig. 5(a)]. This correlation can be physically intuitive, since when the electron density becomes more confined on Mn-3d orbitals, the strength of the on-site Coulomb interactions (U) between these electrons can naturally increase as well, leading to a larger energy penalty for localization. Greater electron lo-

calization on Mn implies a smaller degree of hybridization between Mn and O neighbors, suggesting that the nature of the Mn-O bonding within γ is more ionic, and the bonding within the experimentally known phases is more covalent. Our calculated electronic pDOS of ortho- LiMnO_2 indeed suggests that the Mn-O bonding in this phase is highly covalent in nature, as there is a strong hybridization of Mn-3d and O-2p states within the valence e_g and t_{2g} manifolds near the Fermi level, especially within $r^2\text{SCAN} + U$ and HSE06 (Fig. 8). The disordered layered structure also contains Mn with non-collinear JT distortions and larger values of U , which reflects how the formation of anti-site defects in layered LiMnO_2 can decrease the covalency of some Mn-O bonds. Only the more precise treatments of electronic exchange and correlation within HSE06 and PBEsol + $U_{sc} (+V_{sc})$ can reasonably capture the increase in energy arising from reduced Mn-O covalency, which enables the prediction of significant anti-site defect formation energies.

To clarify the impact of orbital ordering on the electronic properties, we calculate the properties of layered LiMnO_2 with a zig-zag arrangement of JT distortions instead of a collinear arrangement—we will refer to this structure as zz-layered LiMnO_2 ($P2_1/c$ space group), which is shown in

TABLE III. Phonon entropy [$k_B/f.u.$] of the LiMnO_2 phases as a function of temperature.

Temperature (K)	Ortho	Layered	Spinel	ϵ	γ	Disord. Layered	SQS
300	8.26	8.25	8.29	8.26	7.79	7.94	7.97
600	15.45	15.45	15.49	15.44	14.97	15.14	15.19
900	20.08	20.09	20.13	20.08	19.61	19.78	19.82

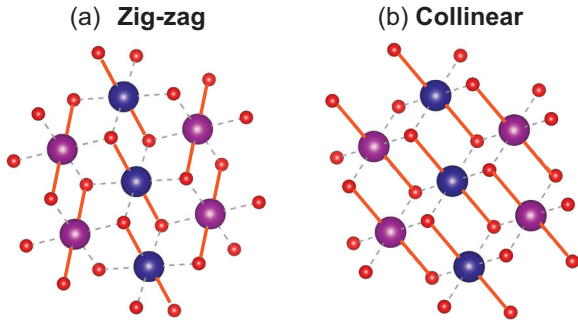


FIG. 11. Structures of AFM layered LiMnO_2 with a) zig-zag ($P2_1/c$) and b) collinear ($C2/m$) ordering of JT axes. Only one Mn layer is shown for clarity. The JT axes are highlighted in orange. Blue - Mn (up spin), purple - Mn (down spin), and red - O.

Fig. 11. The zigzag ordering of JT axes has been previously studied in layered LiMnO_2 and LiNiO_2 [129,130]. We calculate the HPs, Mn magnetic moment, and JT bond ratio of zz-layered within PBEsol + $(U + V)_{\text{sc}}$, and compare them to layered LiMnO_2 in Table IV. Indeed, we find that zz-layered has a self-consistent Hubbard U that is ~ 170 meV larger than layered LiMnO_2 , as well as a larger magnetic moment. In fact, if we use the line of best fit shown in Fig. 5(a) and the computed Mn moment of zz-layered, we can predict a Hubbard U of 6.05 eV, which differs from the self-consistent U only by 0.09 eV. Furthermore, the JT bond ratio of zz-layered is much lower than that of the collinear JT structure, and comparable to γ - LiMnO_2 (Table I). These effects stemming from the collinear JT ordering are thermodynamically favorable, as the computed total energy of the collinear JT ordering is 64–140 meV/Mn lower than the zigzag JT arrangement, depending on the DFT method used (Table S4 [27]). These results provide further evidence that collinear e_g orbital ordering facilitates greater Mn-O covalency and enhances the JT distortion, which results in lowering the total energy.

Our results suggest that the orbital ordering is particularly influential to the phase stability of LiMnO_2 . All structures with a collinear JT ordering exhibit increased covalency of Mn-O bonding, magnitude of JT distortion (Table I), energy differences between the AFM and FM states [up to 100 meV/Mn in ortho and ϵ , shown in Fig. 2(c)], and vibrational entropy (Table III). Thus the JT ordering appears critically linked to several aspects of the electronic and vibrational sources of stability. The LiMnO_2 structures refined from experiment all exhibit the collinear JT ordering [13–15,17–19,117], which further indicates that this cooperative JT effect is indeed very thermodynamically favorable in LiMnO_2 .

TABLE IV. Comparing the properties of layered LiMnO_2 with collinear and zigzag orderings of JT axes—self-consistent Hubbard parameters, Mn moments, and JT bond ratio ($\frac{\text{long}}{\text{avg. short}}$) within PBEsol + $(U + V)_{\text{sc}}$.

Jahn-Teller Ordering	Hubbard U (eV)	Hubbard V (eV)	Mn Moment (μ_B)	JT bond ratio
Collinear ($C2/m$)	5.79	0.65, 0.30	3.38	1.203
Zigzag ($P2_1/c$)	5.96	0.68, 0.60, 0.37	3.41	1.147

We remark that the stability of the collinear JT ordering and its link to other contributions of the phase stability are not ubiquitous to all TM oxides with JT-active ions. In the low-temperature orthorhombic LaMnO_3 perovskite phase, experimental structural refinements have shown that the JT arrangement is noncollinear [131,132]. In previous studies of layered LiNiO_2 , DFT (GGA + U) calculations have shown that the noncollinear zigzag JT ordering is the ground state orbital arrangement [129,130]. Radin *et al.* further showed from GGA + U calculations that the lowering of energy resulting from the JT distortion in layered LiNiO_2 (~ -120 meV/Ni) is much smaller in magnitude than in layered LiMnO_2 (~ -350 meV/Mn) [129]. Furthermore, the stabilizing effect of AFM order in layered LiNiO_2 is predicted to be minimal ($\Delta E_{\text{AFM-FM}} \approx -3$ meV/Ni) [129] compared to layered LiMnO_2 ($\Delta E_{\text{AFM-FM}} \approx -40$ to -60 meV/Mn), which may be largely due to the higher spin state of the Mn^{3+} electron configuration compared to Ni^{3+} .

These discrepancies between layered LiMnO_2 and LiNiO_2 suggest that the contributions to the phase stability of these systems are significantly different. This is indeed reflected in the distinct ground states of these systems—for LiNiO_2 it is the layered structure [10,130], while for LiMnO_2 it is the orthorhombic phase. The orthorhombic phase is unique, as it is the ground state only for LiMnO_2 , while the layered phase is the ground state for many other LiMO_2 compositions ($M = \text{Cr, Co, V, etc.}$) [10]. These observations suggest that the LiMnO_2 phase stability is likely dictated by contributions that are unique to this system, and specifically, the Mn^{3+} ion. Our analysis indicates that these contributions are the strong AFM exchange interactions, collinear JT ordering, increased Mn-O covalency, softening of phonon modes, and the coupling between these factors. The strength of JT distortions and AFM interactions are much greater in LiMnO_2 than in LiNiO_2 , so we suspect that the strength of these contributions may be unique to LiMnO_2 , and indeed helps underpin the unusual phase behavior of this system.

V. CONCLUSION

We have revealed the challenges of modeling the phase stability and electronic structure of the LiMnO_2 polymorphs, and identified avenues for obtaining more accurate results in this system. The degree of electron localization on Mn-3d states is found to vary significantly by phase and is closely correlated to the self-consistently calculated Hubbard U on Mn-3d states. These values of U can vary by ~ 0.6 eV within PBEsol, and are closely linked to the local JT ordering. More conventional DFT approaches (e.g., GGA and meta-GGA with or without averaged Hubbard corrections) inadequately treat the energy differences arising from subtle changes in electron localization and Mn-O bonding, leading to inaccurate phase stability predictions. Instead, more precise treatments of electronic exchange and correlation (and, especially, screened exchange) within functionals such as HSE06, PBEsol + $U_{\text{sc}}(+V_{\text{sc}})$, and $r^2\text{SCAN} + U_{\text{sc}}$ are required to recover more accurate phase stability, namely, the prediction of orthorhombic LiMnO_2 to be the ground state. We expect these DFT methods to be similarly well-equipped to capture the energetics of other TM oxides that are rich in Mn^{3+} or other JT-active ions (e.g., Ni^{3+} and Cu^{2+}).

The ordering of the cations, Mn spins, and e_g orbitals all significantly influence the degree of electron localization and hybridization, which dictate the electronic and vibrational free energy contributions. The collinear arrangement of JT distortions, which is present in ortho, layered, spinel, and ϵ -LiMnO₂, is shown to simultaneously increase the Mn-O covalency, strength of AFM semicovalent exchange, and vibrational entropy compared to structures with noncollinear JT orderings. The subtle interplay between the electron localization, magnetism, JT distortion, and total energy within the LiMnO₂ phases makes this system a potentially useful test case for benchmarking novel density functional approximations.

An extensive re-examination of the electronic structure of ortho-LiMnO₂ reveals the importance of sufficiently correcting the SIE on O-2*p* states, in addition to Mn-3*d* states, in order to obtain accurate features of the band structure, such as the crystal field splitting and band gap. These quantities are well-captured within HSE06, as the predicted band structure is in reasonable agreement with G_0W_0 .

ACKNOWLEDGMENTS

We would like to thank Prof. Steven Louie, Jack McArthur, and other organizing members of the BerkeleyGW workshop for insightful discussion and guidance on *GW* calculations. We also thank Tucker Holstun and Dr. Annalena Genreith-Schriever for valuable discussion about the LiMnO₂ structures and Jahn-Teller distortions, respectively. This work was funded by the U.S. Department of Energy, Office of Science, Office of Basic Energy Sciences, Materials Sciences and Engineering Division under Contract No. DE-AC02-05-CH11231 (Materials Project program KC23MP). This research used computational resources of the National Renewable Energy Laboratory (NREL) and the National Energy Research Scientific Computing Center (NERSC).

DATA AVAILABILITY

The data that support the findings of this article are openly available [92].

-
- [1] J. B. Goodenough and K.-S. Park, The Li-ion rechargeable battery: A perspective, *J. Am. Chem. Soc.* **135**, 1167 (2013).
- [2] M. M. Thackeray, C. Wolverton, and E. D. Isaacs, Electrical energy storage for transportation—approaching the limits of, and going beyond, lithium-ion batteries, *Energy Environ. Sci.* **5**, 7854 (2012).
- [3] Y. Tian, G. Zeng, A. Rutt, T. Shi, H. Kim, J. Wang, J. Koettgen, Y. Sun, B. Ouyang, T. Chen, Z. Lun, Z. Rong, K. Persson, and G. Ceder, Promises and challenges of next-generation “beyond li-ion” batteries for electric vehicles and grid decarbonization, *Chem. Rev.* **121**, 1623 (2021).
- [4] L. Xie, C. Singh, S. K. Mitter, M. A. Dahleh, and S. S. Oren, Toward carbon-neutral electricity and mobility: Is the grid infrastructure ready?, *Joule* **5**, 1908 (2021).
- [5] F. Maisel, C. Neef, F. Marscheider-Weidemann, and N. F. Nissen, A forecast on future raw material demand and recycling potential of lithium-ion batteries in electric vehicles, *Resour. Conserv. Recycl.* **192**, 106920 (2023).
- [6] E. A. Olivetti, G. Ceder, G. G. Gaustad, and X. Fu, Lithium-ion battery supply chain considerations: Analysis of potential bottlenecks in critical metals, *Joule* **1**, 229 (2017).
- [7] M. M. Thackeray, Manganese oxides for lithium batteries, *Prog. Solid State Chem.* **25**, 1 (1997).
- [8] A. Manthiram, J. C. Knight, S. Myung, S. Oh, and Y. Sun, Nickel-Rich and Lithium-Rich layered oxide cathodes: Progress and perspectives, *Adv. Energy Mater.* **6**, 1501010 (2016).
- [9] K. Mizushima, P. Jones, P. Wiseman, and J. Goodenough, Li_xCoO₂ (0 < x < 1): A new cathode material for batteries of high energy density, *Mater. Res. Bull.* **15**, 783 (1980).
- [10] E. J. Wu, P. D. Tepesch, and G. Ceder, Size and charge effects on the structural stability of LiMO₂ (M = transition metal) compounds, *Philos. Mag. Part B* **77**, 1039 (1998).
- [11] S. K. Mishra and G. Ceder, Structural stability of lithium manganese oxides, *Phys. Rev. B* **59**, 6120 (1999).
- [12] G. Dittrich and R. Hoppe, Zur Kristallstruktur von LiMnO₂, *Z. Anorg. Allg. Chem.* **368**, 262 (1969).
- [13] A. R. Armstrong and P. G. Bruce, Synthesis of layered LiMnO₂ as an electrode for rechargeable lithium batteries, *Nature (London)* **381**, 499 (1996).
- [14] F. Capitaine, P. Gravereau, and C. Delmas, A new variety of LiMnO₂ with a layered structure, *Solid State Ionics* **89**, 197 (1996).
- [15] W. David, M. Thackeray, L. D. Picciotto, and J. Goodenough, Structure refinement of the spinel-related phases Li₂Mn₂O₄ and Li_{0.2}Mn₂O₄, *J. Solid State Chem.* **67**, 316 (1987).
- [16] J. Kanamori, Crystal distortion in magnetic compounds, *J. Appl. Phys.* **31**, S14 (1960).
- [17] J. Greedan, N. Raju, and I. Davidson, Long range and short range magnetic order in orthorhombic LiMnO₂, *J. Solid State Chem.* **128**, 209 (1997).
- [18] R. Hoppe, G. Brachtel, and M. Jansen, Zur Kenntnis der Oxomanganate(III):, Über LiMnO₂ und β-NaMnO₂ [1], *Z. Anorg. Allg. Chem.* **417**, 1 (1975).
- [19] J. Akimoto, Y. Takahashi, Y. Gotoh, K. Kawaguchi, K. Dokko, and I. Uchida, Synthesis, crystal structure, and magnetic property of delithiated Li_xMnO₂ (x < 0.1) single crystals: A novel disordered rocksalt-type manganese dioxide, *Chem. Mater.* **15**, 2984 (2003).
- [20] M. Thackeray, W. David, P. Bruce, and J. Goodenough, Lithium insertion into manganese spinels, *Mater. Res. Bull.* **18**, 461 (1983).
- [21] J. N. Reimers, E. W. Fuller, E. Rossen, and J. R. Dahn, Synthesis and electrochemical studies of LiMnO₂ prepared at low temperatures, *J. Electrochem. Soc.* **140**, 3396 (1993).
- [22] R. Gummow, D. Liles, and M. Thackeray, Lithium extraction from orthorhombic lithium manganese oxide and the phase transformation to spinel, *Mater. Res. Bull.* **28**, 1249 (1993).
- [23] R. J. Gummow and M. M. Thackeray, An investigation of spinel-related and orthorhombic LiMnO₂ cathodes for

- rechargeable lithium batteries, *J. Electrochem. Soc.* **141**, 1178 (1994).
- [24] Y.-I. Jang and Y.-M. Chiang, Stability of the monoclinic and orthorhombic phases of LiMnO_2 with temperature, oxygen partial pressure, and Al doping, *Solid State Ionics* **130**, 53 (2000).
- [25] A. R. Armstrong, N. Dupre, A. J. Paterson, C. P. Grey, and P. G. Bruce, Combined neutron diffraction, NMR, and electrochemical investigation of the layered-to-spinel transformation in LiMnO_2 , *Chem. Mater.* **16**, 3106 (2004).
- [26] M. Barré and M. Catti, Neutron diffraction study of the β' and γ phases of LiFeO_2 , *J. Solid State Chem.* **182**, 2549 (2009).
- [27] See Supplemental Material at <http://link.aps.org/supplemental/10.1103/99jn-17v6> for additional details of DFT, linear response calculation of Hubbard parameters, phonon, and cluster expansion calculations; phonon density of states and entropy for each phase, which includes Refs. [34,46,82–84,86–88,90,93,96,102,103,122,123,133–135].
- [28] V. I. Anisimov, J. Zaanen, and O. K. Andersen, Band theory and Mott insulators: Hubbard U instead of stoner I , *Phys. Rev. B* **44**, 943 (1991).
- [29] V. I. Anisimov, F. Aryasetiawan, and A. I. Lichtenstein, First-principles calculations of the electronic structure and spectra of strongly correlated systems: the LDA+ U method, *J. Phys.: Condens. Matter* **9**, 767 (1997).
- [30] J. P. Perdew and A. Zunger, Self–interaction correction to density–functional approximations for many–electron systems, *Phys. Rev. B* **23**, 5048 (1981).
- [31] S. L. Dudarev, G. A. Botton, S. Y. Savrasov, C. J. Humphreys, and A. P. Sutton, Electron-energy-loss spectra and the structural stability of nickel oxide: An LSDA+ U study, *Phys. Rev. B* **57**, 1505 (1998).
- [32] L. Wang, T. Maxisch, and G. Ceder, Oxidation energies of transition metal oxides within the GGA+ U framework, *Phys. Rev. B* **73**, 195107 (2006).
- [33] F. Zhou, M. Cococcioni, C. A. Marianetti, D. Morgan, and G. Ceder, First-principles prediction of redox potentials in transition-metal compounds with LDA + U , *Phys. Rev. B* **70**, 235121 (2004).
- [34] M. Cococcioni and S. Gironcoli, Linear response approach to the calculation of the effective interaction parameters in the LDA+ U method, *Phys. Rev. B* **71**, 035105 (2005).
- [35] H. J. Kulik, M. Cococcioni, D. A. Scherlis, and N. Marzari, Density functional theory in transition-metal chemistry: A self-consistent Hubbard U approach, *Phys. Rev. Lett.* **97**, 103001 (2006).
- [36] V. I. Anisimov, I. V. Solovyev, M. A. Korotin, M. T. Czyżyk, and G. A. Sawatzky, Density-functional theory and NiO photoemission spectra, *Phys. Rev. B* **48**, 16929 (1993).
- [37] V. L. Campo, Jr. and M. Cococcioni, Extended DFT + U + V method with on-site and inter-site electronic interactions, *J. Phys.: Condens. Matter* **22**, 055602 (2010).
- [38] I. Timrov, F. Aquilante, M. Cococcioni, and N. Marzari, Accurate electronic properties and intercalation voltages of olivine-type Li-ion cathode materials from extended hubbard functionals, *PRX Energy* **1**, 033003 (2022).
- [39] L. Binci, M. Kotiuga, I. Timrov, and N. Marzari, Hybridization driving distortions and multiferroicity in rare-earth nickelates, *Phys. Rev. Res.* **5**, 033146 (2023).
- [40] R. Mahajan, I. Timrov, N. Marzari, and A. Kashyap, Importance of intersite Hubbard interactions in $\beta\text{-MnO}_2$: A first-principles DFT+ U + V study, *Phys. Rev. Mater.* **5**, 104402 (2021).
- [41] N. Tancogne-Dejean, M. A. Sentef, and A. Rubio, Ultrafast modification of Hubbard U in a strongly correlated material: *Ab initio* high-harmonic generation in NiO, *Phys. Rev. Lett.* **121**, 097402 (2018).
- [42] B. G. Jang, M. Kim, S.-H. Lee, W. Yang, S.-H. Jhi, and Y.-W. Son, Intersite coulomb interactions in charge-ordered systems, *Phys. Rev. Lett.* **130**, 136401 (2023).
- [43] G. S. Gautam and E. A. Carter, Evaluating transition metal oxides within DFT-SCAN and SCAN+ U frameworks for solar thermochemical applications, *Phys. Rev. Mater.* **2**, 095401 (2018).
- [44] S. Swathilakshmi, R. Devi, and G. S. Gautam, Performance of the r^2 SCAN functional in transition metal oxides, *J. Chem. Theory Comput.* **19**, 4202 (2023).
- [45] V. I. Anisimov and O. Gunnarsson, Density-functional calculation of effective coulomb interactions in metals, *Phys. Rev. B* **43**, 7570 (1991).
- [46] I. Timrov, N. Marzari, and M. Cococcioni, Hubbard parameters from density-functional perturbation theory, *Phys. Rev. B* **98**, 085127 (2018).
- [47] L. Binci and N. Marzari, Noncollinear DFT + U and Hubbard parameters with fully relativistic ultrasoft pseudopotentials, *Phys. Rev. B* **108**, 115157 (2023).
- [48] G. C. Moore, M. K. Horton, E. Linscott, A. M. Ganose, M. Siron, D. D. O'Regan, and K. A. Persson, High-throughput determination of Hubbard U and Hund J values for transition metal oxides via the linear response formalism, *Phys. Rev. Mater.* **8**, 014409 (2024).
- [49] T. Kotani, *Ab initio* random-phase-approximation calculation of the frequency-dependent effective interaction between 3d electrons: Ni, Fe, and MnO, *J. Phys.: Condens. Matter* **12**, 2413 (2000).
- [50] F. Aryasetiawan, M. Imada, A. Georges, G. Kotliar, S. Biermann, and A. I. Lichtenstein, Frequency-dependent local interactions and low-energy effective models from electronic structure calculations, *Phys. Rev. B* **70**, 195104 (2004).
- [51] F. Aryasetiawan, K. Karlsson, O. Jepsen, and U. Schönberger, Calculations of Hubbard U from first-principles, *Phys. Rev. B* **74**, 125106 (2006).
- [52] N. J. Mosey and E. A. Carter, *Ab initio* evaluation of coulomb and exchange parameters for DFT + U calculations, *Phys. Rev. B* **76**, 155123 (2007).
- [53] L. A. Agapito, S. Curtarolo, and M. Buongiorno Nardelli, Reformulation of DFT + U as a pseudohybrid Hubbard density functional for accelerated materials discovery, *Phys. Rev. X* **5**, 011006 (2015).
- [54] S.-H. Lee and Y.-W. Son, First-principles approach with a pseudohybrid density functional for extended Hubbard interactions, *Phys. Rev. Res.* **2**, 043410 (2020).
- [55] M. Yu, S. Yang, C. Wu, and N. Marom, Machine learning the Hubbard U parameter in DFT + U using Bayesian optimization, *npj Comput. Mater.* **6**, 180 (2020).
- [56] G. Cai, Z. Cao, F. Xie, H. Jia, W. Liu, Y. Wang, F. Liu, X. Ren, S. Meng, and M. Liu, Predicting structure-dependent Hubbard

- U parameters via machine learning, *Mater. Futures* **3**, 025601 (2024).
- [57] M. Uhrin, A. Zadoks, L. Binci, N. Marzari, and I. Timrov, Machine learning hubbard parameters with equivariant neural networks, *npj Comput. Mater.* **11**, 19 (2025).
- [58] I. Timrov, M. Kotiuga, and N. Marzari, Unraveling the effects of inter-site Hubbard interactions in spinel Li-ion cathode materials, *Phys. Chem. Chem. Phys.* **25**, 9061 (2023).
- [59] J. Sun, A. Ruzsinszky, and J. P. Perdew, Strongly constrained and appropriately normed semilocal density functional, *Phys. Rev. Lett.* **115**, 036402 (2015).
- [60] J. Sun, R. C. Remsing, Y. Zhang, Z. Sun, A. Ruzsinszky, H. Peng, Z. Yang, A. Paul, U. Waghmare, X. Wu, M. L. Klein, and J. P. Perdew, Accurate first-principles structures and energies of diversely bonded systems from an efficient density functional, *Nat. Chem.* **8**, 831 (2016).
- [61] A. P. Bartók and J. R. Yates, Regularized SCAN functional, *J. Chem. Phys.* **150**, 161101 (2019).
- [62] J. W. Furness, A. D. Kaplan, J. Ning, J. P. Perdew, and J. Sun, Accurate and numerically efficient r²SCAN meta-generalized gradient approximation, *J. Phys. Chem. Lett.* **11**, 8208 (2020).
- [63] R. Kingsbury, A. S. Gupta, C. J. Bartel, J. M. Munro, S. Dwaraknath, M. Horton, and K. A. Persson, Performance comparison of r²SCAN and SCAN metaGGA density functionals for solid materials via an automated, high-throughput computational workflow, *Phys. Rev. Mater.* **6**, 013801 (2022).
- [64] Y. Hinuma, H. Hayashi, Y. Kumagai, I. Tanaka, and F. Oba, Comparison of approximations in density functional theory calculations: Energetics and structure of binary oxides, *Phys. Rev. B* **96**, 094102 (2017).
- [65] J. H. Yang, D. A. Kitchaev, and G. Ceder, Rationalizing accurate structure prediction in the meta-GGA SCAN functional, *Phys. Rev. B* **100**, 035132 (2019).
- [66] D. A. Kitchaev, H. Peng, Y. Liu, J. Sun, J. P. Perdew, and G. Ceder, Energetics of MnO₂ polymorphs in density functional theory, *Phys. Rev. B* **93**, 045132 (2016).
- [67] S. Kümmel and L. Kronik, Orbital-dependent density functionals: Theory and applications, *Rev. Mod. Phys.* **80**, 3 (2008).
- [68] J. Paier, M. Marsman, K. Hummer, G. Kresse, I. C. Gerber, and J. G. Ángyán, Screened hybrid density functionals applied to solids, *J. Chem. Phys.* **124**, 154709 (2006).
- [69] J. Heyd, G. E. Scuseria, and M. Ernzerhof, Hybrid functionals based on a screened Coulomb potential, *J. Chem. Phys.* **118**, 8207 (2003).
- [70] A. V. Krukau, O. A. Vydrov, A. F. Izmaylov, and G. E. Scuseria, Influence of the exchange screening parameter on the performance of screened hybrid functionals, *J. Chem. Phys.* **125**, 224106 (2006).
- [71] V. L. Chevrier, S. P. Ong, R. Armiento, M. K. Y. Chan, and G. Ceder, Hybrid density functional calculations of redox potentials and formation energies of transition metal compounds, *Phys. Rev. B* **82**, 075122 (2010).
- [72] M. C. Toroker, D. K. Kanan, N. Alidoust, L. Y. Isseroff, P. Liao, and E. A. Carter, First principles scheme to evaluate band edge positions in potential transition metal oxide photocatalysts and photoelectrodes, *Phys. Chem. Chem. Phys.* **13**, 16644 (2011).
- [73] F. Hüser, T. Olsen, and K. S. Thygesen, Quasiparticle GW calculations for solids, molecules, and two-dimensional materials, *Phys. Rev. B* **87**, 235132 (2013).
- [74] Z. Ergönenc, B. Kim, P. Liu, G. Kresse, and C. Franchini, Converged GW quasiparticle energies for transition metal oxide perovskites, *Phys. Rev. Mater.* **2**, 024601 (2018).
- [75] M. S. Hybertsen and S. G. Louie, First-principles theory of quasiparticles: Calculation of band gaps in semiconductors and insulators, *Phys. Rev. Lett.* **55**, 1418 (1985).
- [76] M. Shishkin and G. Kresse, Self-consistent GW calculations for semiconductors and insulators, *Phys. Rev. B* **75**, 235102 (2007).
- [77] M. van Schilfgaarde, T. Kotani, and S. Faleev, Quasiparticle self-consistent GW theory, *Phys. Rev. Lett.* **96**, 226402 (2006).
- [78] H. Jiang, R. I. Gomez-Abal, P. Rinke, and M. Scheffler, First-principles modeling of localized *d* states with the GW@LDA + *U* approach, *Phys. Rev. B* **82**, 045108 (2010).
- [79] C. Rödl, F. Fuchs, J. Furthmüller, and F. Bechstedt, Quasiparticle band structures of the antiferromagnetic transition-metal oxides MnO, FeO, CoO, and NiO, *Phys. Rev. B* **79**, 235114 (2009).
- [80] D. J. Singh, Magnetic and electronic properties of LiMnO₂S, *Phys. Rev. B* **55**, 309 (1997).
- [81] J. P. Perdew, A. Ruzsinszky, G. I. Csonka, O. A. Vydrov, G. E. Scuseria, L. A. Constantin, X. Zhou, and K. Burke, Restoring the density-gradient expansion for exchange in solids and surfaces, *Phys. Rev. Lett.* **100**, 136406 (2008).
- [82] G. Kresse and J. Hafner, *Ab initio* molecular dynamics for liquid metals, *Phys. Rev. B* **47**, 558 (1993).
- [83] G. Kresse and J. Hafner, *Ab initio* molecular-dynamics simulation of the liquid-metalamorphous-semiconductor transition in germanium, *Phys. Rev. B* **49**, 14251 (1994).
- [84] G. Kresse and J. Furthmüller, Efficient iterative schemes for *ab initio* total-energy calculations using a plane-wave basis set, *Phys. Rev. B* **54**, 11169 (1996).
- [85] G. Kresse and J. Furthmüller, Efficiency of *ab-initio* total energy calculations for metals and semiconductors using a plane-wave basis set, *Comput. Mater. Sci.* **6**, 15 (1996).
- [86] S. P. Ong, W. D. Richards, A. Jain, G. Hautier, M. Kocher, S. Cholia, D. Gunter, V. L. Chevrier, K. A. Persson, and G. Ceder, Python Materials Genomics (pymatgen): A robust, open-source python library for materials analysis, *Comput. Mater. Sci.* **68**, 314 (2013).
- [87] P. Giannozzi, S. Baroni, N. Bonini, M. Calandra, R. Car, C. Cavazzoni, D. Ceresoli, G. L. Chiarotti, M. Cococcioni, I. Dabo, A. D. Corso, S. d. Gironcoli, S. Fabris, G. Fratesi, R. Gebauer, U. Gerstmann, C. Gougousis, A. Kokalj, M. Lazzeri, L. Martin-Samos *et al.*, QUANTUM ESPRESSO: A modular and open-source software project for quantum simulations of materials, *J. Phys.: Condens. Matter* **21**, 395502 (2009).
- [88] P. Giannozzi, O. Andreussi, T. Brumme, O. Bunau, M. B. Nardelli, M. Calandra, R. Car, C. Cavazzoni, D. Ceresoli, M. Cococcioni, N. Colonna, I. Carnimeo, A. D. Corso, S. d. Gironcoli, P. Delugas, R. A. DiStasio, Jr., A. Ferretti, A. Floris, G. Fratesi, G. Fugallo *et al.*, Advanced capabilities for materials modelling with Quantum ESPRESSO, *J. Phys.: Condens. Matter* **29**, 465901 (2017).
- [89] I. Timrov, N. Marzari, and M. Cococcioni, Self-consistent Hubbard parameters from density-functional perturbation

- theory in the ultrasoft and projector-augmented wave formulations, *Phys. Rev. B* **103**, 045141 (2021).
- [90] I. Timrov, N. Marzari, and M. Cococcioni, HP – A code for the calculation of Hubbard parameters using density-functional perturbation theory, *Comput. Phys. Commun.* **279**, 108455 (2022).
- [91] I. Timrov, F. Aquilante, L. Binci, M. Cococcioni, and N. Marzari, Pulay forces in density-functional theory with extended Hubbard functionals: From nonorthogonalized to orthogonalized manifolds, *Phys. Rev. B* **102**, 235159 (2020).
- [92] Data of the total energies and relaxed structures of each LiMnO₂ phase, computed using various DFT approximations, are released in the MPContribs platform under project `limno2_polymorphs`, <https://doi.org/10.17188/mpcontribs/2568397>.
- [93] L. Barroso-Luque, J. H. Yang, F. Xie, T. Chen, R. L. Kam, Z. Jadidi, P. Zhong, and G. Ceder, Smol: A Python package for cluster expansions and beyond, *J. Open Source Software* **7**, 4504 (2022).
- [94] M. K. Horton, J. H. Montoya, M. Liu, and K. A. Persson, High-throughput prediction of the ground-state collinear magnetic order of inorganic materials using density functional theory, *npj Comput. Mater.* **5**, 64 (2019).
- [95] M. A. Marques, M. J. Oliveira, and T. Burnus, Libxc: A library of exchange and correlation functionals for density functional theory, *Comput. Phys. Commun.* **183**, 2272 (2012).
- [96] A. Togo and I. Tanaka, First principles phonon calculations in materials science, *Scr. Mater.* **108**, 1 (2015).
- [97] P. Zhang, S. G. Louie, and M. L. Cohen, Electron-phonon renormalization in cuprate superconductors, *Phys. Rev. Lett.* **98**, 067005 (2007).
- [98] A. Floris, S. d. Gironcoli, E. K. U. Gross, and M. Cococcioni, Vibrational properties of MnO and NiO from DFT +*U*-based density functional perturbation theory, *Phys. Rev. B* **84**, 161102(R) (2011).
- [99] A. Floris, I. Timrov, B. Himmetoglu, N. Marzari, S. d. Gironcoli, and M. Cococcioni, Hubbard-corrected density functional perturbation theory with ultrasoft pseudopotentials, *Phys. Rev. B* **101**, 064305 (2020).
- [100] G. Petretto, S. Dwaraknath, H. P. Miranda, D. Winston, M. Giantomassi, M. J. v. Setten, X. Gonze, K. A. Persson, G. Hautier, and G.-M. Rignanese, High-throughput density-functional perturbation theory phonons for inorganic materials, *Scientific Data* **5**, 180065 (2018).
- [101] Y. Hinuma, G. Pizzi, Y. Kumagai, F. Oba, and I. Tanaka, Band structure diagram paths based on crystallography, *Comput. Mater. Sci.* **128**, 140 (2017).
- [102] M. S. Hybertsen and S. G. Louie, Electron correlation in semiconductors and insulators: Band gaps and quasiparticle energies, *Phys. Rev. B* **34**, 5390 (1986).
- [103] J. Deslippe, G. Samsonidze, D. A. Strubbe, M. Jain, M. L. Cohen, and S. G. Louie, BerkeleyGW: A massively parallel computer package for the calculation of the quasiparticle and optical properties of materials and nanostructures, *Comput. Phys. Commun.* **183**, 1269 (2012).
- [104] D. Wing, G. Ohad, J. B. Haber, M. R. Filip, S. E. Gant, J. B. Neaton, and L. Kronik, Band gaps of crystalline solids from Wannier-localization-based optimal tuning of a screened range-separated hybrid functional, *Proc. Natl. Acad. Sci.* **118**, e2104556118 (2021).
- [105] M. Camarasa-Gómez, S. E. Gant, G. Ohad, J. B. Neaton, A. Ramasubramaniam, and L. Kronik, Excitations in layered materials from a non-empirical Wannier-localized optimally-tuned screened range-separated hybrid functional, *npj Comput. Mater.* **10**, 288 (2024).
- [106] W. Chen, G. Miceli, G.-M. Rignanese, and A. Pasquarello, Nonempirical dielectric-dependent hybrid functional with range separation for semiconductors and insulators, *Phys. Rev. Mater.* **2**, 073803 (2018).
- [107] F. Sagredo, M. Camarasa-Gómez, F. Ricci, A. Champagne, L. Kronik, and J. B. Neaton, The reliability of hybrid functionals for accurate fundamental and optical gap prediction of bulk solids and surfaces, *J. Chem. Theory Comput.* **21**, 5009 (2025).
- [108] N. E. Kirchner-Hall, W. Zhao, Y. Xiong, I. Timrov, and I. Dabo, Extensive benchmarking of DFT+*U* calculations for predicting band gaps, *Applied Sciences* **11**, 2395 (2021).
- [109] K. Hoang, Defect physics, delithiation mechanism, and electronic and ionic conduction in layered lithium manganese oxide cathode materials, *Phys. Rev. Appl.* **3**, 024013 (2015).
- [110] V. Galakhov, M. Korotin, N. Ovechkina, E. Kurmaev, V. Gorshkov, D. Kellerman, S. Bartkowski, and M. Neumann, Electronic structure of LiMnO: X-ray emission and photoelectron spectra and band structure calculations, *Eur. Phys. J. B* **14**, 281 (2000).
- [111] H. Banerjee, C. P. Grey, and A. J. Morris, Importance of electronic correlations in exploring the exotic phase diagram of layered Li_xMnO₂, *Phys. Rev. B* **108**, 165124 (2023).
- [112] J. B. Goodenough and A. L. Loeb, Theory of ionic ordering, crystal distortion, and magnetic exchange due to covalent forces in spinels, *Phys. Rev.* **98**, 391 (1955).
- [113] J. B. Goodenough, An interpretation of the magnetic properties of the perovskite-type mixed crystals La_{1-x}Sr_xCoO_{3-λ}, *J. Phys. Chem. Solids* **6**, 287 (1958).
- [114] J. B. Goodenough, Theory of the role of covalence in the perovskite-type manganites [La, M(II)]MnO₃, *Phys. Rev.* **100**, 564 (1955).
- [115] P. W. Anderson, Theory of magnetic exchange interactions: Exchange in insulators and semiconductors, *Solid State Phys.* **14**, 99 (1963).
- [116] J. Kanamori, Superexchange interaction and symmetry properties of electron orbitals, *J. Phys. Chem. Solids* **10**, 87 (1959).
- [117] L. Croguennec, P. Deniard, and R. Brec, Electrochemical cyclability of orthorhombic LiMnO₂: Characterization of cycled materials, *J. Electrochem. Soc.* **144**, 3323 (1997).
- [118] J. Reed, G. Ceder, and A. V. D. Ven, Layered-to-spinel phase transition in Li_xMnO₂, *Electrochem. Solid-State Lett.* **4**, A78 (2001).
- [119] J. M. Paulsen and J. R. Dahn, Phase Diagram of Li-Mn-O Spinel in Air, *Chem. Mater.* **11**, 3065 (1999).
- [120] A. Jain, S. P. Ong, G. Hautier, W. Chen, W. D. Richards, S. Dacek, S. Cholia, D. Gunter, D. Skinner, G. Ceder, and K. A. Persson, Commentary: The materials project: A materials genome approach to accelerating materials innovation, *APL Mater.* **1**, 011002 (2013).
- [121] W. Sun, S. T. Dacek, S. P. Ong, G. Hautier, A. Jain, W. D. Richards, A. C. Gamst, K. A. Persson, and G. Ceder, The thermodynamic scale of inorganic crystalline metastability, *Sci. Adv.* **2**, e1600225 (2016).

- [122] A. Zunger, S.-H. Wei, L. G. Ferreira, and J. E. Bernard, Special quasirandom structures, *Phys. Rev. Lett.* **65**, 353 (1990).
- [123] A. v. d. Walle, P. Tiwary, M. d. Jong, D. Olmsted, M. Asta, A. Dick, D. Shin, Y. Wang, L.-Q. Chen, and Z.-K. Liu, Efficient stochastic generation of special quasirandom structures, *Calphad* **42**, 13 (2013).
- [124] G. A. Samara and B. Morosin, Anharmonic effects in KTaO_3 : Ferroelectric mode, thermal expansion, and compressibility, *Phys. Rev. B* **8**, 1256 (1973).
- [125] P. Zhang, W. Luo, V. H. Crespi, M. L. Cohen, and S. G. Louie, Doping effects on the electronic and structural properties of CoO_2 : An LSDA+ U study, *Phys. Rev. B* **70**, 085108 (2004).
- [126] M. D. Radin, J. C. Thomas, and A. Vander Ven, Order-disorder versus displacive transitions in Jahn-Teller active layered materials, *Phys. Rev. Mater.* **4**, 043601 (2020).
- [127] A. J. Millis, Cooperative Jahn-Teller effect and electron-phonon coupling in $\text{La}_{1-x}\text{A}_x\text{MnO}_3$, *Phys. Rev. B* **53**, 8434 (1996).
- [128] E. Pavarini and E. Koch, Origin of Jahn-Teller distortion and orbital order in LaMnO_3 , *Phys. Rev. Lett.* **104**, 086402 (2010).
- [129] M. D. Radin and A. V. d. Ven, Simulating charge, spin, and orbital ordering: Application to jahn-teller distortions in layered transition-metal oxides, *Chem. Mater.* **30**, 607 (2018).
- [130] A. R. Genreith-Schriever, A. Alexiu, G. S. Phillips, C. S. Coates, L. A. V. Nagle-Cocco, J. D. Bocarsly, F. N. Sayed, S. E. Dutton, and C. P. Grey, Jahn-Teller distortions and phase transitions in LiNiO_2 : Insights from *ab initio* molecular dynamics and variable-temperature x-ray diffraction, *Chem. Mater.* **36**, 2289 (2024).
- [131] Q. Huang, A. Santoro, J. W. Lynn, R. W. Erwin, J. A. Borchers, J. L. Peng, and R. L. Greene, Structure and magnetic order in undoped lanthanum manganite, *Phys. Rev. B* **55**, 14987 (1997).
- [132] S.-G. Eriksson, S. Ivanov, J. Eriksen, M. Valkeapää, L. G. Johansson, H. Rundlöf, R. McGreevy, P. Berastegui, P. Björnsson, M. Rubhausen, J. Bäckström, M. Käll, and L. Börjesson, A neutron powder diffraction and inelastic light scattering study of $(\text{La,Sr})\text{MnO}_{3+\delta}$, *Mater. Sci. Forum* **378-381**, 505 (2001).
- [133] G. Prandini, A. Marrazzo, I. E. Castelli, N. Mounet, and N. Marzari, Precision and efficiency in solid-state pseudopotential calculations, *npj Comput. Mater.* **4**, 72 (2018).
- [134] M. v. Setten, M. Giantomassi, E. Bousquet, M. Verstraete, D. Hamann, X. Gonze, and G.-M. Rignanese, The PSEUDODOJO: Training and grading a 85 element optimized norm-conserving pseudopotential table, *Comput. Phys. Commun.* **226**, 39 (2018).
- [135] G. Kresse and D. Joubert, From ultrasoft pseudopotentials to the projector augmented-wave method, *Phys. Rev. B* **59**, 1758 (1999).